

The *Spitzer* View of Low-Metallicity Star Formation: I. Haro 3

Leslie K. Hunt¹, Trinh X. Thuan², Marc Sauvage³, and Yuri I. Izotov⁴

ABSTRACT

We present *Spitzer* observations of the blue compact dwarf galaxy (BCD) Haro 3, with an oxygen abundance of $12 + \log(O/H) = 8.32$. These data are part of a larger study of star formation and dust in low-metallicity environments. The IRS spectrum of Haro 3 shows strong narrow Polycyclic Aromatic Hydrocarbon (PAH) emission, with high equivalent widths. Gaseous nebular fine-structure lines are also seen. Despite the absence of optical high-excitation lines, a faint high-ionization [O IV] line at $25.89\text{ }\mu\text{m}$ indicates the presence of radiation as hard as 54.9 eV. A CLOUDY model suggests that the MIR lines originate in two regions: a low-extinction optically-emitting region, and an optically invisible one with much higher extinction. The morphology of Haro 3 changes with wavelength. IRAC 4.5 μm traces extended stellar photospheric emission from the body of the galaxy and hot dust continuum coming mainly from star-forming regions; 8 μm probes extended PAH emission coming mainly from the general ISM; MIPS 24 and 70 μm images map compact small-grain warm dust emission associated with active star formation, and 160 μm reflects cooler extended dust associated with older stellar populations. We have derived the optical-to-radio spectral energy distribution (SED) of the brightest star-forming region A in Haro 3. The best-fit *DUSTY* model of the SED gives a total luminosity of $2.8 \times 10^9 L_\odot$ and a mass of $2.8 \times 10^6 M_\odot$ for the ionizing clusters. We infer an extinction $A_V \lesssim 3$, intermediate between the optical $A_V \sim 0.5$ and the radio $A_V \sim 8$, consistent with the picture that longer wavelength observations probe more deeply into star-forming regions.

Subject headings: Galaxies: individual: Haro 3; Galaxies: compact; Galaxies: dwarf; Galaxies: starburst; (ISM:) dust, extinction; ISM: lines and bands; Infrared: galaxies; Haro 3

¹INAF-Istituto di Radioastronomia-Sez. Firenze, L.go Fermi 5, I-50125 Firenze, Italy; hunt@arcetri.astro.it.

²Astronomy Department, University of Virginia, P.O. Box 3818, University Station, Charlottesville, VA 22903, USA; txt@virginia.edu

³CEA/DSM/DAPNIA/Service d'Astrophysique, UMR AIM, CE Saclay, 91191 Gif sur Yvette Cedex, France; msauvage@cea.fr

⁴Main Astronomical Observatory, National Academy of Sciences of Ukraine, 03680 Kiev, Ukraine; izotov@mao.kiev.ua

1. Introduction

ISO, together with COBE and SCUBA, has shown convincingly that dusty star formation plays a key role in the early universe. ISOCAM has identified a significant population of dusty active starburst galaxies, the ultraluminous infrared (IR) galaxies (ULIRG), at $z < 1.5$, which account respectively for $\gtrsim 30\%$ and $\sim 10\%$ of the far-IR (FIR) and submm backgrounds (Genzel & Cesarsky 2000), which in turn account for half of the total extragalactic background. Submm observations (e.g., SCUBA, Hughes et al. 1998) suggest that the remaining fractions are also due to ULIRGs, but at higher redshifts ($z > 2$). That dust plays such an important role in the high-redshift universe may appear surprising, as it is usually thought that in the early stages of galaxy formation, when the gas is still relatively metal-free, dust was virtually absent. This assumption however has been challenged by mid-IR (MIR) observations of one of the most metal-poor star-forming galaxies known, SBS 0335–052 E (Thuan, Sauvage, & Madden 1999; Plante & Sauvage 2002; Houck et al. 2004b). In this local blue compact dwarf galaxy (BCD) at a distance of 54 Mpc and with a nebular heavy element abundance of only $12 + \log(\text{O}/\text{H}) = 7.3$, a large amount of dust ($\lesssim 10^5 M_{\odot}$) hides most ($\sim 75\%$) of the current star-forming activity from view (Hunt, Vanzi, & Thuan 2001; Plante & Sauvage 2002; Houck et al. 2004b).

Thus, to interpret the spectra of high-redshift galaxies, it is crucial to understand how and when this ubiquitous dust component is formed and how it affects the spectral energy distribution (SED) of galaxies by redistributing the ultraviolet-optical energy radiated by the young stars in the star-forming regions to MIR and FIR wavelengths. Such an understanding is needed if we are to use these SEDs to derive photometric redshifts and the star formation rate as a function of cosmic epoch. Indeed, the optical-radio SEDs of seven nearby BCDs show several significant deviations from the standard templates of the evolved and massive starbursts (e.g., M 82 and Arp 220) frequently used to derive photometric redshifts of submm/mm sources (Hunt et al. 2005). First, the location of the infrared bump implies generally warmer dust temperatures, with SBS 0335–052 E being the most extreme case of short-wavelength turnover (Houck et al. 2004b; Hunt et al. 2005). Second, the mid-IR spectra of BCDs show very weak or no Aromatic Features in Emission (e.g., PAHs), in contrast to the strong PAH features seen in the spectra of normal starburst galaxies (see also Wu et al. 2006). There is evidence that these characteristics may be more common at high redshift; the SEDs of distant SCUBA/VLA sources tend to be better fit with the SEDs of highly extinguished star clusters (as in the BCD II Zw 40) than with those of M 82 and Arp 220 (Hunt & Maiolino 2005).

Here we present data from our *Spitzer* Cycle 1 program which include spectroscopic, photometric and imaging observations of more than 20 BCDs with metallicities ranging from 1/30 to 1/4 that of the Sun¹. Besides studying the SEDs of BCDs in the infrared, we also wish to investigate star formation in metal-poor environments and how star formation parameters and dust properties change as a function of metallicity. While much progress has been made in finding large popula-

¹ Adopting the solar calibration of Anders & Grevesse (1989).

tions of galaxies at high redshifts ($z \gtrsim 3$ Steidel et al. 2003), truly young galaxies in the process of forming remain elusive in the distant universe. The spectra of those far-away galaxies generally indicate the presence of a substantial amount of heavy elements, indicating previous star formation and metal enrichment. In the hierarchical picture of galaxy formation, large galaxies are formed from the assembly of small ones. Therefore, because of their low mass and chemically unenriched interstellar medium (ISM), BCDs are possibly the closest examples we can find of the elementary units from which galaxies formed. Their relative proximity allows studies of their dust content with a sensitivity, spectral and spatial resolution that faint distant high-redshift galaxies do not permit.

In this first paper of a series, we discuss the most metal-rich object in our sample, Haro 3 = NGC 3353 = Mrk 35. Haro 3 has a heliocentric radial velocity of 969 km s^{-1} (Thuan & Izotov 2005) which gives a distance of 16.3 Mpc , adopting a Hubble constant of $70 \text{ km s}^{-1} \text{ Mpc}^{-1}$ and correcting for the Virgocentric flow. The present distance is about 25% larger than the old distance of 13.1 Mpc used by previous investigators who did not correct for Virgocentric flow. The blue apparent magnitude is of Haro 3 is 13.2 (RC3), which corresponds to a blue absolute magnitude of -17.9 .

With its known population of Wolf-Rayet stars (Steel et al. 1996; Thuan & Izotov 2005), Haro 3 is an ideal object for studying star formation in its relatively early stages. Optical V band observations by Steel et al. (1996) show that Haro 3 hosts several star-forming regions. In order of decreasing brightness, there is first an off-center very blue star-forming region (A: we adopt here the nomenclature of Steel et al. 1996); a nuclear emission region (B); two faint star-forming knots (C) associated with the tidal tail which extends to the south-west of the galaxy; and one or more faint knots to the south (D). These star-forming regions are labeled in the $4.5 \mu\text{m}$ IRAC image of Haro 3 (to be discussed later) in the left panel of Fig. 1. Near-IR (NIR) and high-resolution VLA radio observations by Johnson et al. (2004) demonstrate that the current star formation in Haro 3 is most active in region A, with a star formation rate of $\sim 0.6 \text{ M}_\odot \text{ yr}^{-1}$ and a total mass of young stars of $\sim 10^6 \text{ M}_\odot$ within a region of $\leq 0.1 \text{ kpc}$ radius. Region A is also the youngest star-forming region in Haro 3, with clusters of ages $\lesssim 5 \text{ Myr}$. While the Balmer decrement yields an extinction $A_V = 0.5 \text{ mag}$, Johnson et al. (2004) found that the $\text{Br}\gamma$ and radio fluxes imply a larger extinction in region A, $A_V \sim 8$. As for the clusters in region B, they are slightly older, with ages $\sim 8\text{--}10 \text{ Myr}$ (Johnson et al. 2004). High-resolution *HST*/WFPC2 F606W imaging of Haro 3 by Malkan et al. (1998) shows that regions A and B are separated by a conspicuous dust lane. The various star-forming regions are superimposed on an underlying low-surface-brightness component with somewhat irregular contours, so that Haro 3 is of type iI² in the BCD morphological classification of Loose & Thuan (1985). Its redder color suggests that it is composed of older stars made in previous episodes of star formation. A tidal tail to the south-west is clearly seen in the *HST* image of Malkan et al. (1998), suggesting that some of the present star formation may have been triggered

²iI refers to a complex central structure (star-formation zones not located at or near the center) and outer irregular isophotes. The most common BCD morphology is iE in which the centers show complex structure surrounded by outer circular or elliptical isophotes.

by a merger with another dwarf galaxy or HI cloud. Johnson et al. (2004) proposed that the HI properties of Haro 3 may be suggestive of a small-scale interaction, although higher resolution HI imaging would be necessary to confirm this.

Spectroscopy of region A by Izotov & Thuan (2004) and Thuan & Izotov (2005) gives oxygen abundances of $12+\log(\text{O/H}) = 8.30 \pm 0.01$ and 8.34 ± 0.01 respectively, in good agreement with the value $12+\log(\text{O/H}) = 8.37 \pm 0.06$ obtained earlier by Steel et al. (1996). If we adopt $12+\log(\text{O/H}) = 8.32$ and a solar oxygen abundance of $12+\log(\text{O/H}) = 8.91$ (Anders & Grevesse 1989), Haro 3 would have a metallicity of about 1/4 that of the Sun. If, instead, we adopt the new solar calibration of Asplund et al. (2005) with $12+\log(\text{O/H}) = 8.65$, then Haro 3 would have a metallicity of 1/2 solar.

We describe our new *Spitzer* observations and their reduction in Section 2. In Section 3, we present the spectroscopic results, and discuss the PAH features and the IR fine-structure lines. We also compare the observed IR emission-line intensities with those predicted by a CLOUDY (Ferland 1996; Ferland et al. 1998) photoionization model based on the observed optical emission line fluxes. The IR morphology of the star formation in Haro 3 is described in Section 4. In Section 5, we construct a SED of Haro 3 from $1\,\mu\text{m}$ to $3.6\,\text{cm}$ based on our *Spitzer* and literature data. Grain properties and characteristics of the brightest emission region are derived by fitting the SED with a *DUSTY* model (Ivezić & Elitzur 1997; Ivezić et al. 1999). We discuss Haro 3 in a general context in Section 6 and summarize our conclusions in Section 7.

2. Observations and Data Reduction

As part of our Cycle 1 *Spitzer* proposal (PID 3139: P.I. Thuan), we have observed Haro 3 with IRS (Houck et al. 2004a) in the low- and high-resolution modules (SL, SH, LH); with IRAC (Fazio et al. 2004) at 4.5 and $8\,\mu\text{m}$; and with MIPS (Rieke et al. 2004) at 24 , 70 , and $160\,\mu\text{m}$. The data were acquired over a period of several months on 17 Nov 2004 (IRS), 23 Nov 2004 (IRAC), and 3 Apr 2005 (MIPS). For all instruments, we started the data reduction with images processed by the *Spitzer* Science Center (SSC) pipeline, i.e. the Basic Calibrated Data (*bcd*) and the corresponding masks (the DCE masks). The masks flag potential spurious features in the images, such as strong radiation hits, saturated pixels, or nonexistent/corrupted data.

2.1. IRS Spectra

Spectroscopy was performed in staring mode with the Short Low module in both orders (SL1, SL2) and with both Short and Long High-resolution modules (SH, LH) (Houck et al. 2004a). These give low-resolution spectra from 5.2 to $14.5\,\mu\text{m}$ ($R \simeq 64\text{--}128$), and high-resolution spectra from 9.6 to $37.2\,\mu\text{m}$ ($R \simeq 600$). We obtained $30\text{s} \times 4$ cycles for SH, $14\text{s} \times 8$ for LH, $6\text{s} \times 3$ for SL1, and $6\text{s} \times 6$ for SL2. Sources were centered in the slits by peaking up and offsetting from 2MASS stars. Figure 2 shows

the positions of the three different slits across Haro 3; in the left panel, the slits are superimposed on the *HST*/WFPC2 F606W image (Malkan et al. 1998) and in the right panel on the $H\alpha$ image of Gil de Paz et al. (2003). It can be seen that all three slits include region A.

It is necessary to accurately subtract the background before spectrum extraction. Because of the dominance of the background signal, the accuracy of this process strongly influences the quality of the final spectrum. We started the spectral reduction with the individual *bcd* frames processed by the S11.0.2 version of the SSC pipeline, which provides ramp fitting, dark current subtraction, droop and linearity corrections, flat-fielding, and wavelength and flux calibrations³. However, the pipeline does not include background subtraction. Hence, for the low-resolution spectra, we constructed a coadded background frame from the *bcd* observations with the source in the opposing nod and off-order positions (see also Weedman et al. 2005). When the source is in SL1, the SL2 slit samples background, and vice versa. This makes it possible to include the off-order frames in the background image since the same on-chip integration times were used for both SL orders. The image for the source at a given nod position was constructed by coadding all frames at that position. Coadding was performed with the sigma-clipping option of the *imcombine* task in IRAF⁴. The inclusion of off-order and off-nod frames in the background image means that the integration time on the background is three times that on the source, which improves the signal-to-noise of the two-dimensional (2D) subtraction.

For the high-resolution SH and LH spectra, a 2D background image could not be constructed because of the small size of the slit. Therefore we subtracted the background from the SH and LH observations using the one-dimensional (1D) spectra as described below. The SH and LH 2D *bcd* images were coadded as for the SL modules, and successive corrections for sporadic bad pixels and cosmic ray hits were carried out manually by inspection of the images at the separate nod positions.

We extracted the source spectra with *SPICE*, the post-pipeline IRS package furnished by the SSC. To maximize the calibration accuracy, the automatic point-source extraction window was used for all modules. The automatic extraction uses a variable-width extraction window which scales with wavelength in order to recover a constant fraction of diffraction-limited instrument response. For the SL spectra, this gives a 4-pixel (7''.2) length at $6\mu\text{m}$, and an 8-pixel one (14''.4) at $12\mu\text{m}$; the slit width is 3''.6 for both SL modules. At high resolution, the *SPICE* extraction is performed over the entire slit (4''.7 \times 11''.3 SH; 11''.1 \times 22''.3 LH). Orders were spliced together by averaging, ignoring the noisy regions at the red end of each order (e.g. Armus et al. 2004). Then the individual spectra were box-car smoothed to a resolution element, and clipped in order to eliminate any remaining spikes in the high-resolution data. Finally, the two spectra for each module (one for each nod position) were averaged.

³See the IRS Data Handbook, <http://ssc.spitzer.caltech.edu/irs/dh>.

⁴IRAF is the Image Analysis and Reduction Facility made available to the astronomical community by the National Optical Astronomy Observatory, which is operated by AURA, Inc., under contract with the U.S. National Science Foundation.

Background was subtracted from the 1D SH spectra by minimizing the difference between the 2D background-subtracted SL and SH spectra over the substantial ($\sim 5 \mu\text{m}$) overlap in wavelength. We adopted the model of Reach and coworkers⁵ for the spectral shape of the background, and the multiplicative constant was given by the minimization. The LH background was subtracted by minimizing the difference between the SH and LH spectra over their overlap region ($\lesssim 1 \mu\text{m}$).

The final averaged IRS spectra obtained in the short-wavelength low-resolution mode (SL) and in both short and long wavelength high-resolution modes (SH, LH) are shown in Fig. 3.

2.2. IRAC Images

We designed our IRAC Astronomical Observation Requests (AORs) to give four (high-dynamic range⁶) IRAC frames of 30s; only channels 2 ($4.5 \mu\text{m}$) and 4 ($8.0 \mu\text{m}$) were acquired. Small-scale dithering in a “cycling” pattern was performed with a total of 120s spent in each IRAC channel.

The individual *bcd* frames were processed with the S11.0.1 version of the SSC pipeline (see the IRAC Data Handbook⁷). This processing is designed to remove the effects of dark current, detector nonlinearity, flat field, multiplexer bleeding, and cosmic rays, and to perform flux calibration. However, in some cases, those with particularly bright sources in the field-of-view, the pipeline is unsuccessful at removing all artefacts. In the case of Haro3, the bright point-like source at the center of the galaxy resulted in a “banding” effect in the $8 \mu\text{m}$ image, i.e. in an artificially enhanced brightness level in the rows and columns containing that bright source (see the IRAC Data Handbook). The $4.5 \mu\text{m}$ image was not affected by banding since it occurs only in the Si:As arrays (channels 3 and 4). Dithering does not eliminate the effect because the position of the bands on the array remains unchanged relative to the galaxy. Moreover, because the intensity of the brightness enhancement decreases with distance from the bright source, it is not straightforward to correct automatically. We eliminated the effect from each $8 \mu\text{m}$ frame by interpolating the feature across the affected rows, substituting the spurious pixel values with those of a typical background.

The *bcd* frames (corrected for “banding” effects in the case of the $8 \mu\text{m}$ ones) were coadded using *MOPEX*, the image mosaicing and source-extraction package provided by the SSC (Makovoz & Marleau 2005). Pixels flagged by the DCE masks and by the static bad-pixel masks (pmasks) were ignored. Additional inconsistent pixel values were removed by means of the *MOPEX* outlier rejection algorithms. We relied on the dual-outlier technique, together with the multiframe algorithm, rather than using any spatial criteria for rejection. The frames were corrected for geometrical distortion and projected onto a “fiducial” (refined) coordinate system with pixel sizes

⁵See <http://ssc.spitzer.caltech.edu/documents/background>.

⁶This AOR option gives two sets of four frames each: one with the specified integration time, and one with a shorter time, typically $\sim 1\text{s}$.

⁷Available from the SSC website <http://ssc.spitzer.caltech.edu/irac/dh/>

of $1''.20$, roughly equivalent to the original pixels. Standard linear interpolation was used for the mosaics. The noise levels in our post-pipeline *MOPEX* mosaics are comparable to or lower than those in the SSC products. The final coadded 4.5 and $8.0\,\mu\text{m}$ images are shown respectively in the left and right panels of Fig. 1. We also show $4.5\,\mu\text{m}$ contours superimposed on the *HST*/WFPC2 F606W image of Malkan et al. (1998) in Fig. 4. Examination of Fig. 4 shows that the $4.5\,\mu\text{m}$ peak coincides with the bright optical point source associated with the compact radio emission (Johnson et al. 2004).

2.3. MIPS Images

Our MIPS images were acquired in the Fixed Cluster-Offset mode in all three channels, with offsets of $12''$ in two additional pointings. We used ramp times of 3s, 10s, and 10s for $24\,\mu\text{m}$, $70\,\mu\text{m}$, and $160\,\mu\text{m}$, respectively, with 1, 2, and 6 cycles in the three channels. This gave us a total of 32 frames at $24\,\mu\text{m}$, 56 frames at $70\,\mu\text{m}$, and 104 frames at $160\,\mu\text{m}$. Because the first data frame of each observation sequence at $24\,\mu\text{m}$ has a shorter exposure time, we discarded those frames with keyword DCENUM=0; we also removed the second frame (DCENUM=1) because of increased data artefacts (see the MIPS Data Handbook⁸); this left us with 24 frames at $24\,\mu\text{m}$.

The individual *bcd* frames were processed by the S11.4.0 version of the SSC pipeline, which converts the integration ramps inherent to the MIPS detectors into slopes, and remediates temporal variation of the slope images (Gordon et al. 2005). The processing includes correcting for stimulator flashes on the MIPS-Ge detectors, dark subtraction, flat-fielding, and flux calibration. As for the IRAC images, we processed the dithered *bcd* frames in the spatial domain with *MOPEX*. The DCE masks and the static masks were used to flag pixels, and subsequently ignore them. The *MOPEX* outlier rejection was used to flag any additional spurious pixel values, with the dual-outlier and multiframe algorithm as for the IRAC frames. Geometrical distortion was corrected before projecting the frames onto a fiducial coordinate system with pixel sizes of $1''.20$ for MIPS-24, roughly half of the original pixel size of $2''.5$. Pixel sizes of the final mosaics at 70 and $160\,\mu\text{m}$ are also approximately half of the originals, i.e. $4''.95$ at $70\,\mu\text{m}$ and $8''.0$ at $160\,\mu\text{m}$. Unlike the IRAC coadds, we incorporated the sigma-weighting algorithm because we found it gave less noisy MIPS mosaics than without. Standard linear interpolation was used in all cases. In all three channels, our post-pipeline *MOPEX* mosaics are superior to those provided by the automated post-pipeline reduction. The final coadded images are shown in Fig. 5 as contours superimposed on the *HST*/WFPC2 (left panel) and on the IRAC $8\,\mu\text{m}$ images (right panel).

⁸ Available from the SSC website <http://ssc.spitzer.caltech.edu/mips/dh/>

2.4. IRAC and MIPS Photometry

We have performed aperture photometry on the IRAC and MIPS images with the IRAF photometry package *apphot*, taking care to convert the MJy/sr flux units of the images to integrated flux. The background level was determined by averaging several adjacent empty sky regions. The photometric growth curves are shown in Fig. 6, for IRAC in the left panel, and for MIPS in the right panel. We have also made photometric measurements of the instrument point response functions (PRFs), provided in the *MOPEX* package⁹; the dashed lines show the growth curve expected from a point source, normalized to the total flux indicated by horizontal dotted lines in Fig. 6.

Inspection of Fig. 6 shows that Haro 3 is clearly extended at IRAC wavelengths (4.5 and 8 μm), and possibly at 160 μm , but appears virtually point-like at 24 and 70 μm . The morphology of the 24 μm image is essentially that of a point source (see Fig. 5). To check for source extension, we have fitted elliptical gaussians to the brightest source in the IRAC and MIPS-24 images. The width (equal to the gaussian σ) of these fits is $\gtrsim 2''.4$ in both the IRAC and MIPS-24 images, which implies that, indeed, the source is quite extended at IRAC wavelengths, but more point-like at 24 μm . However, at 24 μm , the diffraction limit is $\sim 6''$, implying that the gaussian fit is too narrow; moreover the 24 μm flux resulting from this fit may be too low (see §5), because the fit does not account for the substantial flux in the first Airy ring. The fraction of total flux contained in the gaussian-like source is 40%, 30%, and 58%, at 4.5, 8.0, and 24 μm , respectively. The total IRAC and MIPS fluxes are given in Table 1, along with other published near-infrared, far-infrared and radio photometry on Haro 3. For the *Spitzer* photometry, we adopt a global uncertainty of 10%, which should account for the various contributions to the uncertainties, including flux calibration and imperfect sky subtraction.

2.5. Comparison With Previous Work

Haro 3 was observed with the *Infrared Space Observatory (ISO)* by Metcalfe et al. (1996) and by the *Infrared Astronomy Satellite (IRAS)* (Table 1). The flux measured in the *ISO* LW6 filter (7–8.5 μm) of 149 ± 30 mJy is in excellent agreement with the total flux of 148 mJy measured in the 8 μm channel of IRAC. The total flux of 300 ± 70 mJy given by Metcalfe et al. (1996) in the *ISO* 12–18 μm LW3 filter is also consistent with the IRS spectrum, considering that Haro 3 is slightly extended at these wavelengths. The IRS spectrum levels generally agree well with other measurements, implying that the background subtraction is reliable.

Our measured *Spitzer* 24 μm total flux of 810 ± 81 mJy agrees well with the *IRAS* flux of 942 ± 57 mJy at 25 μm . The MIPS long-wavelength fluxes at 70 and 160 μm of ~ 3.9 Jy are slightly

⁹We used the most recent determinations of the PRFs dated 5 October 2005.

lower than the *IRAS* fluxes of 4.9 (60 μm) and 6.7 (100 μm) Jy taken from NED¹⁰. But given that they are measured in smaller apertures, our fluxes are consistent with those of *IRAS*. We conclude that our measurements are in general good agreement with previous existing data and that we can have confidence in our reduction procedures. We next discuss how our *Spitzer* data, combined with optical, near-infrared and radio data, can constrain the properties of the stellar populations, the ionized gas and the dust, and help us to construct a picture of the star formation in Haro 3.

3. Spectroscopic results

Polycyclic Aromatic Hydrocarbon (PAH) emission from small dust grains and gaseous nebular line emission are visible in the IRS spectrum of Haro 3 (Fig. 3). These features are superimposed on a steeply rising continuum which peaks around $\sim 100 \mu\text{m}$ ¹¹.

3.1. PAH Features

Examination of the IRS spectra in Fig. 3 shows that there are PAH features clearly detected at 5.7, 6.2, 7.7, 8.6, 11.2, 12.7, and 16.4 μm . We have derived the flux and equivalent width (EW) of these features by fitting the SL and SH spectra with a series of lorentzian profiles of unknown width, amplitude, and central wavelength. Because of their broad low-intensity wings, the PAH features are better fit with lorentzian than with gaussian profiles. The fits were performed with the *splot* task in *IRAF*. The continuum was linearly interpolated in two sections, one from 6-9 μm , and the other from 10.5-13.9 μm . The best-fit parameters, averaged over several independent estimates in both high and low resolution spectra, are given in Table 2. The flux of the 12.7 μm PAH feature is probably overestimated because of the difficulty in separating it from the bright [Ne II] fine structure line (see §3.2).

Our derived values are in general agreement with those based on *ISO* spectra (Metcalfe et al. 1996). There is however a large difference in the slope of the continuum between the ISOPHOT and IRS spectra. The ISOPHOT continuum is nearly flat while the IRS one is continuously rising toward longer wavelengths (Fig. 3). We interpret this continuum slope difference as due to the fact that different regions in Haro 3 are sampled by ISOPHOT and IRS, as a result of the different apertures in the two instruments. The *ISO* PHT-S beam is $25'' \times 25''$ ($\sim 2 \text{kpc}$), considerably larger than the IRS apertures. For the latter, the slit width is $3''.6$ for both SL modules, while it is $4''.7 \times 11''.3$ for the SH module and $11''.1 \times 22''.3$ for the LH module. This means that, while the IRS apertures include mainly radiation from the star-forming region A, the *ISO* aperture encompasses

¹⁰The NASA/IPAC Extragalactic Database (NED) is operated by the Jet Propulsion Laboratory, California Institute of Technology, under contract with the National Aeronautics and Space Administration.

¹¹This is where the flux distribution peaks (see Table 1); the SED (energy distribution) peaks at $\sim 40 \mu\text{m}$.

a large part of the interstellar medium (ISM) around region A. So the spectrally flat PAH emission seen by ISOPHOT comes from the general extended ISM in Haro 3 while the strong rising MIR continuum emission seen by IRS is related to the more compact star-forming region A.

The relative strengths of the three main PAH emission features can be used as diagnostics to identify PAH sizes and infer the neutral-to-ionized gas ratio (Draine & Li 2001). According to the models of Draine & Li (2001) and the observed flux ratios of the $f_{11.2}/f_{7.7}$ and $f_{6.2}/f_{7.7}$ features, the PAHs in Haro 3 are predominantly neutral and small, containing a few hundred carbon atoms, similar to the normal galaxies studied by Helou et al. (2000). In other words, Haro 3 lies in the “normal galaxy” region in the PAH diagnostic diagram rather than in the starburst galaxy region which includes objects such as M82 and NGC 253, that are dominated by ionized PAHs. This again supports our previous contention that the PAHs in Haro 3 arise mainly from the normal ISM around the star-forming region, not only from knot A itself.

On the other hand, the PAH EWs are generally high, ~ 2.9 for the $7.7\mu\text{m}$ line, more typical of starburst galaxies (Brandl et al. 2004) than of BCDs (Wu et al. 2006). This result may not be surprising as Haro 3 with $M_B = -17.9$ is at the bright end of the luminosity function of dwarf galaxies, but it contrasts with the flux ratio trends described above. Overall, Haro 3 follows the metallicity trends of increasing PAH EW with increasing oxygen abundance reported by Wu et al. (2006) and discussed by Hogg et al. (2005) and Engelbracht et al. (2005). However, for its metallicity, the EWs of the ionized PAHs in Haro 3 exceed by $\sim 50\%$ to up to almost a factor of three that of most extreme BCD in the Wu et al. (2006) sample. In contrast, the neutral PAH at $11.2\mu\text{m}$ has an EW of 0.6, typical of other BCDs.

Finally, we find that the PAH emission features in Haro 3 are narrow, narrower than many of the objects tabulated by Li & Draine (2001). The only objects which possess PAH features with smaller widths at $7.7\mu\text{m}$ are the Small Magellanic Cloud, the reflection nebulae/photodissociation region NGC 7023, and 30 Doradus in the Large Magellanic Cloud. M82 and NGC 253 have slightly broader PAH features than these objects or Haro 3, but the difference may not be significant. However, different PAH features tend to have systematically different FWHMs (Li & Draine 2001), so that to make a more definitive statement, we must wait for more data and a more uniform method of measuring PAH parameters (e.g., *PAHFIT*: Smith et al. 2006). Perhaps not surprisingly, Haro 3’s PAH features are also narrower than those predicted by the model for the diffuse Galactic ISM at high latitudes (Li & Draine 2001). We have tried to subtract a scaled version of the model spectrum from the observed spectrum of Haro 3, but because of the narrowness of the features and their lower equivalent widths (because of the rising continuum), the scaled subtraction leaves significant residuals. We conclude that there are many factors behind the appearance of PAH features (e.g., chemical abundance, ISM energetics, etc.). Thus even though our IRS spectrum may contain a conspicuous ISM component, Galactic ISM spectra may not be a good template for all ISM PAH emission.

3.2. Infrared Fine-Structure Lines

The spectrum also shows several fine-structure lines, including the highest signal-to-noise detections $[\text{S IV}]\lambda 10.51$, $[\text{Ne II}]\lambda 12.81$, $[\text{Ne III}]\lambda 15.55$, 36.01, $[\text{S III}]\lambda 18.71$, 33.58, $[\text{O IV}]\lambda 25.89$, and $[\text{Si II}]\lambda 34.82\mu\text{m}$. As for the PAH features, we used *splot* to fit the IR fine-structure emission lines and obtain fluxes and EWs. A deblending procedure was adopted to accurately measure the emission lines at wavelengths near PAH features (e.g., $[\text{Ar III}]$ and $[\text{Ne II}]$). Unlike the PAHs, the lines were best fit with a gaussian profile. A single continuum was linearly interpolated from 10.5 to $\sim 15\mu\text{m}$. For the longer wavelengths, the local continuum was fit by linearly interpolating over adjacent line-free regions. The fluxes and other parameters resulting from the fits are reported in Table 3.

Several fairly high-excitation lines are detected in Haro 3. The $[\text{O IV}]$ line at $25.89\mu\text{m}$ is faint, but present. $[\text{O IV}]$ is a high excitation line, with an excitation potential of 54.9 eV, just beyond the HeII edge at 54 eV. Its detection is consistent with the Wolf-Rayet population present in Haro 3's starburst (Steel et al. 1996; Thuan & Izotov 2005). Thuan & Izotov (2005) have looked in the optical spectrum of Haro 3 for the high-ionization $[\text{Fe V}]\lambda 4227$ and $\text{HeII}\lambda 4686$ nebular emission lines which both have an ionization potential of 54.4 eV. None were seen. Evidently, the observed optical ionizing radiation is less hard than that in the MIR range. This may suggest the presence of substantial extinction in the blue, or indicate that the optical and MIR radiations come from different locations in the star-forming region A, or both (see also §3.3 and §5).

Line ratios of different ionic species of the same element, e.g., $[\text{Ne III}]$ and $[\text{Ne II}]$, are sensitive to the shape of the ionizing radiation field. The ratio of the $[\text{Ne III}]$ and $[\text{Ne II}]$ lines is 2.8, placing Haro 3 toward the high-excitation end of the starbursts studied by Verma et al. (2003), and similar to NGC 5253. Because PAHs tend to be depleted in hard radiation fields, their EW would be expected to be negatively correlated with the $[\text{Ne III}]/[\text{Ne II}]$ line ratio. Such a trend was indeed found by Wu et al. (2006) for their BCD sample. However, compared to the Wu et al. (2006) correlation, the PAHs in Haro 3 tend to have higher EWs for their metallicity than other BCDs. This may again be due to a significant PAH component from the general ISM in Haro 3 as compared to the BCDs studied by Wu et al. (2006), as the region of Haro 3 encompassed by the IRS slit is relatively large, about 500 pc. It could also arise from different measurement techniques, as Wu et al. (2006) fit a spline to the underlying continuum, while we linearly interpolate over two sections of “global” continua.

We can estimate the electron density with the temperature-insensitive $[\text{S III}]$ lines. The flux ratio $f_{33.84}/f_{18.71}$ is 2.5, well into the low-density limit (Draine 2006). The implied electron density is $\lesssim 100\text{ cm}^{-3}$, lower than the optically-derived value of $180\pm 30\text{ cm}^{-3}$ by Izotov & Thuan (2004) from the $[\text{S II}]\lambda 6717/\lambda 6731$ ratio. Even with a maximum uncertainty on the $[\text{S III}]$ flux ratio of $\sim 20\%$, these two densities are inconsistent. Beam dilution could be affecting the MIR line ratios, since the IRS aperture is several times larger than the optical one. Alternatively, this discrepancy could be again suggesting that the optical emission comes from a different spatial location in the

star-forming region A as compared to the MIR emission.

3.3. CLOUDY Models

Since the amount of hard radiation and the electron number density implied from the optical and MIR spectra appear to differ, it is interesting to ask whether we can construct a photoionization model which is consistent with *both* the optical and MIR line intensities. The photoionization model will concern only region A as both the optical and MIR slits include only that region. Radio observations of Johnson et al. (2004) show it to be composed of two main sources (A1 and A2) and a third much fainter one (A3), separated by the angular distance $\sim 1''$. Therefore, optical and MIR spectra in fact include the contribution of all three regions because of the relatively large apertures. All three sources are thermal, indicating that the radio emission is from HII regions.

To construct a photoionized HII region model of region A, we have used the CLOUDY code (version c05.07, Ferland 1996; Ferland et al. 1998). We first ran a series of models assuming that both the optical and the MIR light originate in the same region, characterized by the Balmer-decrement derived extinction ($A_V = 0.52$ mag). While entirely consistent with the optical line emission, these simple models underestimate the MIR line fluxes by factors of 5 or more.

We then developed a series of two-component models: region A1 characterized by the Balmer-decrement derived extinction ($A_V = 0.52$ mag), and region A2, invisible in the optical. The implicit assumption here is that the extinction A_V in A2 is $\gtrsim 6$ mag or so, consistent with the absence of A2 in the *HST* optical image (Johnson et al. 2004). Hence, only A1 contributes to the optical emission, while both A1 and A2 contribute to the emission in the MIR. We neglect the contribution of region A3 as it is much less luminous than regions A1 and A2. The dust responsible for the extinction is assumed to lie *outside* of the HII region, rather than mixed with the ionized gas.

The parameters of the HII region model for A1 were adjusted such that it best reproduces the optical nebular emission-line intensities in Haro 3 as observed by Izotov & Thuan (2004). Several input parameters are needed for this. The first is the observed flux of the $H\beta$ emission, corrected for the optically derived extinction $A_V = 0.52$ mag, of 4.59×10^{-13} erg s $^{-1}$ cm $^{-2}$. This corresponds to a $H\beta$ luminosity $L(H\beta) = 1.45 \times 10^{40}$ erg s $^{-1}$, or a number of ionizing photons $Q_{\text{Lyc}} = 3.05 \times 10^{52}$ s $^{-1}$. The latter value is consistent with that derived by Johnson et al. (2004) for region A1 from the VLA radio continuum observations (after adjusting the distance). Another input parameter is the ionizing stellar radiation. We incorporate a Costar model (Schaerer & de Koter 1997) with a SED corresponding to that of a main-sequence star with an effective temperature of 40600 K. We adopt a spherical ionization-bounded HII region model with an inner radius of 10^{19} cm, a constant density of 100 cm $^{-3}$, and a filling factor of 0.005. The chemical composition of the HII region is shown in Table 4. Only three parameters are fixed: Q_{Lyc} , the filling factor, and the gas number density. All other parameters were varied to obtain the best coincidence of the observed and modeled line intensities in the optical range (Table 5). With this model for A1, we obtain

good or reasonable agreement for nearly all the optical line intensities. They correspond in general to element abundance ratios typical of solar ones except for a slightly lower N/O abundance ratio. The exception is iron. To fit the observed [Fe III] $\lambda 4658, \lambda 5270$ emission lines, we needed to adopt a Fe/O abundance ratio which is about one order of magnitude lower than the solar one. This suggests that iron is highly depleted in Haro 3, probably onto dust grains, implying the presence of a significant amount of dust in Haro 3. Our subsequent estimate of the dust mass (§5) confirms this conclusion.

For region A2, we have no constraints in the optical range for its H II region model. Therefore, we adopt for this region the same parameters as for region A1 except for the number of ionizing photons Q_{LyC} (i.e., $H\beta$ luminosity) and filling factor. According to Johnson et al. (2004) Q_{LyC} for A2 is 1.5 times greater than for region A1. Thus, we assume that the intrinsic, i.e. extinction-corrected, flux of the $H\beta$ emission line in region A2 is 1.5 times greater than that in region A1. As for the filling factor, we adopt it to be 0.0025 in region A2, lower than that for A1, because of the more diffuse morphology of A2 in the radio map by Johnson et al. (2004).

The 05.07 version of CLOUDY includes the calculation of line intensities in the MIR range. We combine both models for regions A1 and A2 to fit the observed intensities of the MIR lines. In Table 6, we compare the observed and predicted intensities of the MIR lines listed in Table 3. Columns 2 and 5 show the observed and predicted intensities for regions A1+A2 relative to the (intrinsic) total $H\beta$ intensity for both regions. Columns 3 and 4 give the predicted intensities of emission lines normalized to the respective intensities of $H\beta$ in each of regions A1 and A2. Column 6 is the ratio of observed (column 2) to predicted (column 5) line intensity. It is seen that the observed intensities of the majority of the MIR lines, with the exception of the $[\text{Ne II}]\lambda 12.81 \mu\text{m}$ and the $[\text{Ne III}]\lambda 36.01 \mu\text{m}$ lines, are ~ 1.7 times higher than the predicted ones.

The Spitzer/IRS aperture is significantly larger than the narrow slit of $2''.0$ used in the optical observations, so that aperture effects could explain part of the discrepancy. We can estimate the discrepancy factor potentially due to aperture effects by using the total observed $H\alpha$ flux of $2.75 \times 10^{-12} \text{ erg s}^{-1} \text{ cm}^{-2}$ measured by Gil de Paz et al. (2003) on an $H\alpha$ image of Haro 3. With the observed $H\alpha/H\beta$ ratio of 3.47 in the optical slit, and the uncorrected $H\beta$ flux of $2.6 \times 10^{-12} \text{ erg s}^{-1} \text{ cm}^{-2}$, we obtain an uncorrected (for extinction) $H\alpha$ flux of $9.1 \times 10^{-13} \text{ erg s}^{-1} \text{ cm}^{-2}$; this value is about three times smaller than the total flux measured by Gil de Paz et al. (2003). We have also measured the fraction of the $H\alpha$ emission in the Gil de Paz et al. (2003) image which falls in the IRS slits (see right panel of Fig.2). Because of the orientation of the slits and their different sizes, roughly 36% of the total $H\alpha$ emission lies within the SL slit; $\approx 25\%$ within the SH slit; and $\approx 80\%$ within LH. Diffraction effects have not been considered here, so such estimates are rather crude. Moreover, the optical line emission suffers from highly variable extinction, which would result in relatively less $H\alpha$ flux in the more obscured region A2. All things considered, we conclude that aperture effects could account for the discrepancies for most lines in Table 6.

The discrepancy between the observed and predicted intensity ratios of the two weakest lines,

$[\text{Ne II}]\lambda 36.01 \mu\text{m}$ and $[\text{Ne II}]\lambda 12.81 \mu\text{m}$, are larger than for the others. In part, this discrepancy could be explained by the observational errors, at least in the case of the weakest $[\text{Ne III}]\lambda 36.01 \mu\text{m}$ emission line. Indeed, the observed ratio $[\text{Ne III}]\lambda 15.55 \mu\text{m} / [\text{Ne III}]\lambda 36.01 \mu\text{m}$ of ~ 6 is a factor of two greater than the predicted one. As for the $[\text{Ne II}]\lambda 12.81 \mu\text{m}$ emission line, its intensity was obtained with a deblending algorithm from the high-resolution IRS SH spectrum (see §3.2) because of its proximity with the $12.7 \mu\text{m}$ PAH feature. Even with the high-resolution IRS spectrum, this deblending is not straightforward, and the $[\text{Ne II}]$ line could consequently be overestimated.

Thus, taking into account a high extinction for region A2, aperture corrections and possible sources of the uncertainties for the weakest MIR lines, we find an overall good agreement between the observed intensities of the optical and MIR lines. We conclude that the MIR lines probe a region which has more extinction than the location where the optical lines originate. This hypothesis will be confirmed later by our *DUSTY* calculations.

4. The Infrared Morphology of Haro 3

We now use the Spitzer IRAC (Fig. 1) and MIPS (Fig. 5) data to study the origin of the infrared emission in Haro 3. Fig. 1 shows that both the $4.5 \mu\text{m}$ (IRAC2) and $8.0 \mu\text{m}$ (IRAC4) emissions are extended on galaxy scales (see also the growth curves of as compared to the point-spread function in Fig. 6). They follow well the optical features as shown in Fig. 4, and the optical knots A–D are all detected. In particular, the IRAC emission peaks on region A, coincident with the strong compact radio source seen by Johnson et al. (2004), the site of the most active star-forming region in Haro 3.

4.1. The PAH Component

Emission in the IRAC bands is the sum of three different components: 1) the stellar photospheres, 2) the hot dust continuum, and 3) the PAHs. Because of the usual dominance of the PAHs in MIR spectra of star-forming galaxies (see the Haro 3 MIR spectrum in Fig. 3), the $8 \mu\text{m}$ IRAC channel is commonly used as a “PAH indicator” (Hogg et al. 2005; Engelbracht et al. 2005). The $4.5/8.0$ flux ratio is thus a potentially important diagnostic for characterizing the ISM properties at short wavelengths: high $4.5/8.0$ ratios would indicate predominantly stellar light, whereas low ratios would point to a relatively large PAH contribution.

An IRAC $4.5/8.0$ color image was created from the two IRAC 4.5 and $8 \mu\text{m}$ mosaics by first subtracting the background measured in empty regions in each mosaic, then aligning the two mosaics by cross correlation, and finally dividing one by the other. The result is shown in the right panel of Fig. 4 where the $4.5 \mu\text{m}$ image contours are superimposed on the $4.5/8.0 \mu\text{m}$ flux ratio map. Inspection of Fig. 4 shows that the $4.5/8$ flux ratio varies by more than a factor of 10 over the galaxy, with peaks $\gtrsim 0.5$ and troughs of $\lesssim 0.1$. Because the $4.5/8.0$ color of stellar populations is

~ 2.5, roughly independently of age and metallicity (Leitherer et al. 1999), it is clear the the color map of Haro 3 is dominated by the ISM, and not by stars. The only source with 4.5/8.0 colors near the stellar value is knot D to the south of the nucleus (there is no $H\alpha$ emission associated with this object).

If we interpret the $8\mu\text{m}$ emission in the IRAC band in the “standard” way and attribute it primarily to PAHs, the low 4.5/8 ratio ~ 0.1 around knots A and B (see Fig. 4) would imply a substantial PAH contribution. Indeed this interpretation is supported by the detection of strong PAH features in the IRS spectrum (see §3). If all the changes in the 4.5/8 ratio over the galaxy were attributed only to changes in the PAH emission, the higher ratio ~ 0.3 in the broad “ridge” to the southeast of the nucleus (see Fig. 4) would indicate that PAHs should be *three times less prominent* there. It could be that the PAHs are destroyed by the radiation fields in the star-forming regions associated with the intense circumnuclear $H\alpha$ visible in the right panel of Fig. 2.

4.2. The Hot Dust Continuum

On the other hand, the spatial variations in the 4.5/8 flux ratio could be associated with variations in the hot dust $4.5\text{--}8\mu\text{m}$ continuum. As pointed out by Wu et al. (2006) and others, variations in the $8\mu\text{m}$ continuum can masquerade in broadband images as variations in the PAH contribution. Because in Haro 3 the PAHs and continuum contribute roughly equally to the $8\mu\text{m}$ filter¹², it is not unreasonable to think that the larger 4.5/8 μm ratios are due to a flatter continuum slope, i.e. a lower $8\mu\text{m}$ continuum, in the general extended ISM as compared to star-forming region A.

We can test this hypothesis by making IRAC/MIPS hybrid color images. Since the IRAC $4.5\mu\text{m}$ image traces stars and hot dust but not PAH features, the IRAC $8\mu\text{m}$ image mainly the dust continuum and PAHs with a very small stellar contribution, and the MIPS $24\mu\text{m}$ image the warm or hot dust continuum only, we should be able to use the IRAC/MIPS colors to distinguish between continuum and PAH variations. Since the Spitzer diffraction limit is $1''.11$ at $4.5\mu\text{m}$, $1''.98$ at $8\mu\text{m}$ (see the IRAC Data Handbook), and $\sim 6''$ at $24\mu\text{m}$, comparison of the IRAC 4 and $8\mu\text{m}$ images with the MIPS $24\mu\text{m}$ image is only possible after some processing of the latter. The availability of an accurate PRF makes possible a deconvolution for the MIPS-24 image, which we performed with the *lucy* task in the *STSDAS*¹³ extension of *IRAF*, using the *MIPS24_PRF_mosaic* in the *mopex* distribution as the deconvolution kernel. Prior to deconvolution, the MIPS image

¹²This is indeed the case for region A: we decomposed the IRS spectrum into a sum of lorentzian functions for the PAH bands and a continuum and synthesized from this model the IRAC $8\mu\text{m}$ flux, to show that each component contributes the same amount of energy in the band.

¹³*STSDAS* is the Space Telescope Science Data Analysis System, distributed by the Space Telescope Science Institute, which is operated by the Association of Universities for Research in Astronomy (AURA), Inc., under NASA contract NAS 5-26555.

was linearly interpolated to the finer pixel scale of the PRF. After deconvolution, the image was rebinned to the original scale of the MIPS 24 μm mosaic (see §2.3), designed to be the same as the IRAC scale. The original and deconvolved MIPS-24 images are shown in Fig. 7. Just as we did for the IRAC color maps, background was first subtracted for the IRAC and MIPS images, then the images were aligned using a cross correlation technique, and finally the IRAC image was divided by the MIPS image. The 4/24 μm and 8/24 μm flux ratios obtained from the deconvolved 24 μm images are shown in Fig. 8 where the 4.5 μm image is superimposed in contours.

There are several features of the hybrid IRAC/MIPS-24 color images in Fig. 8 to be noticed. First, the high ratio of ~ 0.6 in source A in the 8/24 color map is much larger than the value inferred from the IRS spectrum of ~ 0.06 . However the spectrum has not been deconvolved and is roughly diffraction limited at all wavelengths. This means that it encompasses a larger fraction of the extended source as wavelength increases. At $\sim 8 \mu\text{m}$ the spectrum encompasses a region of $\sim 2''$ in size, while at $24 \mu\text{m}$ it encompasses a $\sim 6''$ region. Therefore, it is likely that the higher image value is closer to the true one for region A than the low value derived from the IRS spectrum which is more typical of the general ISM. Indeed, the value of the 8/24 color averaged over a 40'' square region is ~ 0.17 , consistent with the color derived from total fluxes. Hence, we believe that the general structure of the hybrid IRAC/MIPS-24 color images is reliable.

Second, as mentioned before, there is a noticeable feature with a high 4.5/8 ratio (~ 0.3) tracing a broad ridge to the southeast of region A (see the right panel of Fig. 4). Our aim is to use the 24 μm map to trace the hot dust continuum, and compare it to the IRAC colors. The ridge feature is also present in the 4.5/24 and 8/24 color maps (Fig. 8). However, because of its location, the feature in the 24 μm map ratios may be an artefact of the deconvolution procedure. To check its reality, we have performed three tests. First, we have convolved the IRAC 8 μm image with the MIPS-24 PRF and then divided the resulting image by the original 24 μm image. Second, we have convolved the MIPS-24 deconvolved image with the IRAC 8 μm PRF and divided by the original 8 μm image. Third, we have divided the original 24 μm image by its PRF. The results of the first and third tests are shown in Fig. 9. The second test is not shown: because of the small size of the IRAC PRF, the color image obtained this way is virtually indistinguishable from the one made with the MIPS-24 deconvolved image. Inspection of Fig. 9 shows that the feature of interest in the 24 μm map coincides roughly with the Airy wings of the MIPS-24 PRF. Thus the broad ridge in the 24 μm map ratios may not be a real feature; this means that the 24 μm image cannot be used to unequivocally validate either hypothesis for the red 4.5/8 μm ridge color.

Nevertheless, we can examine the relative colors of the ridge and the surrounding disk. First, the *ridge* in Haro 3 has a 4.5/8 flux ratio of ~ 0.28 , “bluer” than the surrounding *disk* with $\sim 0.12 - 0.15$. If the change in color depends solely on the 8 μm band, then the ridge would have to have either 50% fewer PAHs or 50% less hot dust at 8 μm than the disk. Since we expect the disk to have less hot dust than any actively star-forming region, we must necessarily conclude that the “ridge” is deficit in PAHs, not in the hot dust continuum. The PAHs could have been destroyed because of proximity to the edge of the ionized gas shell (see $H\alpha$ image in Fig. 2), or by supernovae

shocks and outflows perpendicular to the dust lane.

The morphology of the 4/24 and 8/24 flux ratio maps as shown in Fig. 8 is complex; both ratios vary by a factor of $\gtrsim 30$ over the galaxy, being greatest in and around knot C toward the southwest and knot D toward the southeast. Because knot D has R -band emission, but no $H\alpha$ in the images by Gil de Paz et al. (2003), the reason for its high 4/24 and 8/24 ratios is unclear; indeed we cannot exclude that knot D be merely a foreground star. On the other hand, in knot C, we tentatively interpret these high ratios to be due to *increased* PAH strength, or equivalently, *decreased* hot dust. First, the 4.5/8 flux ratio in knot C is half that in knots A and B, and the morphology in the color is clearly extended. Second, both the 4.5/24 and 8/24 ratios are also lower in knot C. Hence, we conclude that there is less hot dust emitting at $4.5\mu\text{m}$ and $8\mu\text{m}$ in knot C than in knots A and B, and possibly an $8\mu\text{m}$ PAH excess.

The difficulty of separating PAH and continuum contributions in the broadband IRAC $8\mu\text{m}$ filter is evident from the above discussion. In Haro 3, with its conspicuous $H\alpha$ emission throughout the entire central region and across the dust lane, the ISM changes from predominantly neutral in the outer disk to ionized in the inner regions. Because of the complex morphology from 5 to $8\mu\text{m}$ on kpc scales, we conclude that the ISM has been disturbed by the combined effects of the star-formation episodes concentrated in knots A, B, and C.

4.3. The Cool Dust Continuum

Fig. 5 shows the dust emission at the longer wavelengths of 24, 70 and $160\mu\text{m}$. The emission at 24 and $70\mu\text{m}$ is virtually point-like, and appears to be mainly associated with the most active star-forming region A. The point-like nature of the 24 and $70\mu\text{m}$ emission is also illustrated by the growth curves in Fig. 6¹⁴. However, the emission at $160\mu\text{m}$ appears to be more extended (see also its growth curve in Fig. 6).

Like most other galaxies, Haro 3 is a composite entity in the IR; we see different components and morphologies depending on wavelength. In Haro 3, we see *extended* stellar photospheric and *compact* hot dust continuum emission at $4.5\mu\text{m}$; *extended* PAH emission in the general ISM at $8\mu\text{m}$ but with some hot dust continuum and stars; *compact* warm dust emission associated with active star-forming regions at 24 and $70\mu\text{m}$; and cooler *extended* dust emission associated with older stellar populations at $160\mu\text{m}$.

¹⁴The $24\mu\text{m}$ flux given by the gaussian fit discussed in §2.4 is too low relative to the spectrum. The MIPS-24 image of Haro 3 resembles the octagonal shape of the PRF, which is strongly diffraction limited with a pronounced Airy ring. Hence, we would expect a gaussian fit to give a lower flux than the true one, since it does not include the flux in the Airy maximum at radii of $\sim 6''$, and may also have overestimated the background because of the additional emission at these radii.

5. Modeling the Infrared Spectral Energy Distribution of Region A in Haro 3

We now use the complete IR SED to constrain the properties of the star formation and the dust in the brightest star-forming region in Haro 3, region A. The infrared morphology revealed by the IRAC and MIPS images (Fig. 1 and 5) suggest that region A dominates the SED of Haro 3 at wavelengths $20 \lesssim \lambda \lesssim 100 \mu\text{m}$. The IR SED of this region, a strong continuum with ionic lines indicating a relatively hard ionizing source, is quite similar to that observed toward dust-enshrouded super star clusters, such as for instance in NGC 5253 (see Vanzi & Sauvage 2004, and references within). Such an identification is confirmed by the detection of compact thermal radio emission from region A by Johnson et al. (2004), emission identified as originating in the compact HII region created by the star cluster.

5.1. Fitting with *DUSTY*

To constrain the properties of this cluster and its surrounding dust envelope, we have fit the NIR-FIR SED of this source with the radiative transfer code *DUSTY* (Ivezić et al. 1999; Ivezić & Elitzur 1997). *DUSTY* solves the radiative transfer problem in a dust envelope but has a number of limitations which must be understood so we can properly evaluate the results it gives. First, *DUSTY* assumes a spherically symmetric dust envelope which is decoupled from the ionizing radiation source. While this decoupling is probably realistic for the stars and the dust (we do not expect much of the dust to survive in or very near the star cluster), it is much less so for the ionized gas which is a source of radiation through its continuum emission, and the dust. The assumption of spherical symmetry is also too strong to be realistic. Second, *DUSTY* assumes that grains are in thermal equilibrium with the radiation field. This may be the case for all grains near and in the cluster exposed to its intense and hard radiation, but clearly not so for grains in the general interstellar medium of Haro 3. These two limitations mean that the SED we can fit realistically with *DUSTY* concerns only region A, but not the whole galaxy.

To construct the SED of region A, we must use high spatial resolution observations in order to distinguish its emission from emission from other parts of Haro 3. In the NIR, which is a useful domain to constrain the total optical depth to the cluster, we use the NIR observations listed in Table 1, taken from Johnson et al. (2004). Given that our IRS spectrum is centered on region A and includes the spectral region covered by our IRAC data, we have preferred to use the IRS rather than the IRAC data in the 5-35 μm range. We however do not use the IRS spectrum in its original form but rather in its PAH-subtracted version. As explained earlier, the PAH component in the original IRS spectrum is related to the general ISM of Haro 3 and therefore not relevant here. The MIPS point at 24 μm is included in the fit, although it does not provide supplementary constraints with respect to the IRS spectrum. As the 70 μm MIPS image is strikingly pointlike we assume that it is entirely due to region A. The 160 μm MIPS image is more extended than the PSF (Fig. 6) and therefore likely contains a contribution from the general ISM. However it is not possible to

accurately deconvolve the $160\,\mu\text{m}$ image to derive the point-source component flux only. We thus should keep in mind in judging the goodness of the fit that the $160\,\mu\text{m}$ flux is likely an upper limit to the actual flux from region A.

The IRAS and ISO measurements of Haro 3 were not used in the fit for two reasons. First, the ISO fluxes and the IRAS 12 and $25\,\mu\text{m}$ fluxes fall in a region of the SED that is better covered by the IRS and MIPS data, and including them does not add more information. Comparison of the IRAS 60 and $100\,\mu\text{m}$ fluxes to the MIPS 70 and $160\,\mu\text{m}$ fluxes shows that, although they are compatible with each other within their respective error bars, the IRAS photometry is systematically higher than the MIPS photometry. This can be due either to the larger IRAS beam since it subtends more faint extended emission than the smaller Spitzer beam or to an incorrect cross-calibration between IRAS and Spitzer. At this stage of the Spitzer mission, cross-calibration with another mission can indeed be uncertain and, as a result we rather restrict ourselves to the Spitzer data. Finally, the radio data of Johnson et al. (2004), although of very high spatial resolution, were not used in the fit because first, *DUSTY* does not take into account radio emitting processes; and second, the contribution of free-free and synchrotron emission to the SED at the longest wavelength point ($160\,\mu\text{m}$) is negligible.

Before proceeding with the fit, we recall that region A is composite. It is composed of two main sources (A1 and A2) and a much fainter third one (A3). Making a single *DUSTY* model for a collection of identical sources is not a problem since the total values of the quantities of interest such as opacities, luminosities and masses, are independent of the actual number of sources used to fit the SED. However, as discussed before, A1 and A2 are not identical (we will neglect the faint A3). Thus, A2 has no optical counterpart in the *HST* F606W band image while A1 does. It is also not clear that the Br γ and radio emission in the direction of A2 come from the same source, while such an association is much clearer in A1. Finally, the different derivations of the extinction toward region A (essentially A1+A2) by Johnson et al. (2004), using the radio to Br γ ratio, the hydrogen Balmer line ratios, and the NIR colors, disagree. While this is a rather common situation, it points to a non-homogeneous extinction in region A and suggests that A1 and A2 may not be in the same “evolutionary” stage. Indeed, our CLOUDY modeling does suggest that A2 has more extinction than A1 (§3.3). This composite nature of region A must be kept in mind when discussing the physical properties deduced from the fit. This is however the best we can do: the lack of high resolution data in the MIR-FIR allows us only to make a single *DUSTY* model of the SED of region A which includes both A1 and A2.

When judging the goodness of the fit, it is also important to compare the number of independent constraints with the number of model parameters. For practical purposes we have integrated the IRS data in a series of 10 pseudo-filters with a resolving power $\lambda/\Delta\lambda$ of 5. The NIR data consists of three bands, while MIPS provides 2 independent measurements. We therefore have 15 independent constraints on the fit. The model requires a large number of parameters. We need first to specify a heating source. We take it to be described by the Starburst99 (Leitherer et al. 1999, hereafter SB99) burst stellar populations at the metallicity of Haro 3. This requires one parameter,

the age of the burst. The dust is described by its composition and size distribution. We take it to be formed of silicates, graphites and amorphous carbons. Thus the dust mix requires two more parameters. The dust size distribution is characterized by a minimum and a maximum size and a power law exponent, requiring three additional parameters. The dust shell around the star cluster is modeled as a series of embedded shells, each with an outer (relative) radius and an exponent for the power-law describing the dependence of the dust density on radius. Thus the total number of parameters required is $2 \times N_{\text{shell}}$. The “size” of the system is described by the temperature at the inner edge of the first shell. Finally the total amount of dust is constrained by the optical depth at V. A complete *DUSTY* model is therefore described by $8 + 2 \times N_{\text{shell}}$, i.e. in principle, a model with 3 shells is still over-constrained by the data.

To estimate the goodness of fit of a model, we compute the quantity:

$$\sigma = \sum_{\text{filter } i=1}^{\text{filter } i=N} w_i \times \left[\log(f_i^{\text{obs}}) - \log(f_i^{\text{mod}}) \right]^2, \quad (1)$$

where f_i^{obs} and f_i^{mod} are respectively the observed and modeled fluxes, the latter being obtained by convolving the SED with the appropriate filter bandpasses, and w_i is a weight defined as:

$$w_i = \frac{1}{R_i^{\text{pow}}} \times \frac{N}{\sum_{\text{filter } i=1}^{\text{filter } i=N} \frac{1}{R_i^{\text{pow}}}} \quad (2)$$

Here, R_i^{pow} is the resolving power $\lambda/\Delta\lambda$ of each filter or pseudo-filter.

The weighting scheme is designed to reflect the fact that a broadband filter in the NIR collects the same amount of information as a broadband filter in the FIR, although their widths are very different. The sum of the weights is normalized to N, the number of filters used to construct the SED.

To search for the best fitting dust SED, i.e. the one with the lowest σ , we have run about 3×10^6 *DUSTY* models, varying N_{shell} from 1 to 3. The optical depth τ_V is varied from 0 to 50, with most of the exploration being done in the range 0 to 30, with steps of 1 or 2. The minimum and maximum dust grain sizes are varied within the range between 0.001 and 40 μm , with the minimum sizes clustered around 0.01 μm and the maximum sizes clustered around 1 μm ; the steps are generally logarithmic, varying from a 10% increase to a factor of 2. The exponent of the size distribution is varied within the range [0-4.5] with most of the models in the range [2.5-4]. Typical steps are 0.5. The temperature on the inner side of the dust shell ranged from 10 K to 1600 K, with most of the models in the range 400 K to 700 K, and typical steps are 25-50 K. Only 3-component dust mixes were investigated (with silicates, graphites and amorphous carbons), with their proportions varying uniformly in the range 0-100%. Steps in the proportions vary between 1% to 30%. 1.6 million 1-zone models were explored, with the outer radius varying from 25 to 1000 in an uniform manner and with a density exponent ranging between 0 and 2. We ran also just short of a million 2-zone models where the outer radius was varied between 100 and 1000, and the intermediate radius

between 2 and 999. In these models the density exponent ranged between -2 and 4 , with most values between -1 and 2 . About 3.5×10^5 3-zone models were run, where the outer radius was fixed at 1000 and the intermediate radius sampled the range from 10 to 999 uniformly. In the 3-zone models, the density exponent was varied from -1 to 3 with a large number of models between 0 and 1 . Steps in radius are between 25 and 50 , and steps in the density exponent are 0.5 .

5.2. Results

The parameters of the best-fit *DUSTY* model are listed in Table 7 and the resulting SED is displayed in Fig. 10. The σ of this model is 0.015 , which implies a mean ratio between the model and observed fluxes of $\sim 7\%$, well within the observational errors. Uncertainties in the parameters (last column in Table 7) are estimated by exploring the range where σ is degraded to 10% . From the *DUSTY* fit, it is possible to reconstruct physical parameters such as the size of the system, the bolometric luminosity, and the dust mass, following the methods described in Plante & Sauvage (2002) and Hunt et al. (2005).

5.2.1. The Ionizing Star Cluster

As always in such a fit, the best constrained quantity is the bolometric luminosity of the system. This is because, for a well-sampled SED, this luminosity being the integral of the SED, the observed and best-fit ones should be the same. The luminosity of the model is $2.8 \times 10^9 L_\odot$. This is quite a large luminosity for a single cluster however, as discussed before, we are quite likely dealing in this case with at least two clusters (A1 and A2). The bolometric luminosity constitutes a large but not unreasonable fraction of the total galaxy luminosity: for comparison, the $8\text{--}1000\,\mu\text{m}$ luminosity derived from the IRAS bands (Sanders & Mirabel 1996) is $4.1 \times 10^9 L_\odot$. With the bolometric luminosity of the system, we can then use the SB99 models to derive several physical parameters of the central ionizing source. The best-fit SED corresponds to a SB99 model with a Salpeter Initial Mass Function and a burst age of $5\,\text{Myr}$. As this SB99 cluster has a luminosity of $10^9 L_\odot$ for a stellar mass of $10^6 M_\odot$, the ionizing source has then a mass of $2.8 \times 10^6 M_\odot$. This is again in the high mass range for stellar clusters, but acceptable given that region A is a multiple source.

The best-fit age for the cluster is $5\,\text{Myr}$, in the upper range of ages that have been derived for region A using various diagnostics. For example, in the course of a large program to determine electron temperatures of HII regions in BCDs by fitting their optical SEDs ($3200\text{--}5200\,\text{\AA}$) and in particular the Balmer jump ($\lambda 3646\,\text{\AA}$), Guseva, Izotov & Thuan (2006) have determined the stellar populations of a number of galaxies, including region A in Haro 3. They approximate the star formation history of region A by two bursts of different strengths, a recent burst with an age $t(\text{young})$ to account for the young stellar population and a prior burst with an age $t(\text{old})$ responsible

for the older stars. The contribution of each burst to the SED is given by the ratio of the masses of stellar populations formed respectively in the old and young bursts, $b = M(\text{old})/M(\text{young})$. The contribution of gaseous emission is determined from the observed equivalent width of the $H\beta$ emission line $\text{EW}(H\beta)$. Those authors ran a large number (10^5) of Monte Carlo models varying simultaneously $t(\text{young})$, $t(\text{old})$ and b . They found that the model which best fits the SED of Haro 3 has $t(\text{young}) = 4$ Myr, $t(\text{old}) = 2$ Gyr and $b = 20$. The age of the young burst so derived is in good agreement with the one of ~ 5 Myr derived by Johnson et al. (2004) from fitting the NIR colors, and the one derived here by the *DUSTY* fit.

SB99 predicts also the number of hydrogen-ionizing photons Q_{LyC} from such a cluster. We find $Q_{\text{LyC}} \sim 4.4 \times 10^{52}$ photons s^{-1} . This is on the low side of the range of values for A1+A2 given by Johnson et al. (2004), i.e. from 4.3 ($B\gamma\gamma$) to 8.2×10^{52} photons s^{-1} (radio) converted to the distance used here. Johnson et al. (2004) interpret the disagreement between the two derivations of Q_{LyC} as a sign for the existence of highly obscured sources in region A. This explanation cannot account for our low value of Q_{LyC} : since we reproduce the full SED of region A, there is no room for extra sources as they would inevitably contribute substantial emission in some wavelength range. A possible explanation could be that the age we derive is too old. As can be seen in Leitherer et al. (1999) a 2.5 Myr cluster has a Q_{LyC} 5 times higher while its total luminosity has only increased by a factor 1.5. Yet a more likely explanation is related to the composite nature of region A: A1 seems to suffer from very little extinction, while A2 seems to be more obscured. One could thus envision a situation where the less obscured source is indeed a 5 Myr cluster, though less luminous than we find here, while the more obscured source is a younger cluster. Such a model however has too many free parameters to be constrained by the data at hand.

5.2.2. The Dust Cloud

The derived properties of the dust “shell” around the ionizing clusters lead to a more surprising picture. The first intriguing feature concerns the nature of the dust. We find that silicates are absent from the best-fitting chemical mix. This situation is similar to that in NGC 5253 (Vanzi & Sauvage 2004) where modeling of the embedded star cluster also indicates a lack of silicates. This situation likely results from the need for significantly hot dust to produce the NIR continuum, while avoiding the generation of silicate emission/absorption features which would be expected from small hot silicate grains in an optically thick regime. If the hot dust continuum were produced by thermally fluctuating small carbon grains, then colder silicate dust grains may exist in the outer part envelope. However these two features – stochastic heating, and a radial dependence of the chemical composition – are not implemented in *DUSTY*.

The second intriguing feature concerns the size of the grains. To reproduce the full SED, and in particular its FIR part, the maximum grain size must exceed $\sim 11 \mu\text{m}$; the upper limit to the largest possible size is unconstrained by our fit. Even though the best-fit value is large, $\sim 40 \mu\text{m}$, this is still small compared to the millimeter-sized grains that have been advocated to fit

the SEDs of circumstellar shells (see e.g. Men'shchikov et al. 2002), this is quite large compared to the standard MRN size distribution (Mathis et al. 1977), with a maximum size of $0.25\text{-}1.0\,\mu\text{m}$. If we allow the fit to the $160\,\mu\text{m}$ MIPS flux to be significantly worse since it is likely an upper limit, we can relax the constraint on the largest grain size to values that are more consistent with the MRN distribution. Unlike the maximum size, the minimum size and the exponent of the size distribution are very similar to the MRN distribution.

The last surprising feature concerns the extent and mass of the “shell”: at the adopted distance of $16.3\,\text{Mpc}$, it has a radius of $430\,\text{pc}$, considerably larger than region A and nearly reaching region B (Fig. 4). A more detailed look at the model reveals that, despite the large extent of the dust shell, the other physical parameters are not unreasonable. First, with $\tau_V = 3$, the shell needs not be very thick. In fact, it is not truly a shell since the density shows no dependence with radius, i.e. the exponent of the density power law distribution is equal to zero. Thus, the geometry deduced from the *DUSTY* modeling is more that of a large cloud of dust surrounding region A than that of a giant dust shell. One could in fact consider that the best fitting model describes, not so much an embedded cluster and its envelope, but the general ISM of Haro 3 heated locally by the clusters in region A. This would make region A an example of the later stage in the possible evolutionary sequence that goes from totally embedded super-star clusters to completely unobscured ones (e.g. Calzetti et al. 1997). The IRAC and the shorter-wavelength MIPS images do not show such an extended dust cloud because of the presence of temperature and hence surface brightness radial gradients in Haro 3. In the model, the energy source lies at the center, the surface brightness is centrally peaked and the apparent size of the object is smaller than its physical size. At $160\,\mu\text{m}$, with a resolution of $\sim 40''$, Haro 3 appears extended (resolved), which would be consistent with the cool dust temperature at a radius of $430\,\text{pc}$. *DUSTY* can compute images at selected wavelengths; these images reveal that the FWHM of the dust cloud is always smaller than the instrumental PSF 24 and $70\,\mu\text{m}$. Therefore although the model dust cloud is large, it would not necessarily be seen as a resolved object in the 24 and $70\,\mu\text{m}$ images. At $160\,\mu\text{m}$ however, with a resolution of $\sim 40''$, Haro 3 appears slightly resolved, which is not the case of the model cloud. This probably indicates that a fraction from the $160\,\mu\text{m}$ flux is not heated by region A but rather finds its energy source in the general interstellar radiation field.

We derive an opacity $\tau_V = 3$ from our best-fit model. In the model context, this is the optical depth of the “shell” toward the central source. There are many possible explanations of the difference between the *DUSTY*-derived optical depth τ and the measured values of the extinction A from recombination lines. The simple and linear relation between the two quantities ($A \sim 1.086\,\tau$) is only valid in the screen geometry, when scattering and radiation transfer are neglected. Although *DUSTY* assumes a screen geometry, it treats the complete radiation transfer process: absorption, scattering, and re-emission of the absorbed energy. As scattering has a wavelength dependence opposite to that of extinction, the resulting relation between A and τ becomes shallower and depends strongly on wavelength. Another plausible explanation is that a more realistic geometry would have part of the source region, and in particular the ionized gas responsible for all the lines

and for a large fraction of the NIR emission, mixed with the absorbing dust. This also results in a shallower relation between A and τ . In any case, the model value of A_V is within the range of observationally determined values of A_V . From the optical recombination lines, Thuan & Izotov (2005) derive $A_V = 0.5$. Comparing $B\gamma$ from Johnson et al. (2004) with $H\beta$ gives $A_V = 0.9$. From the location of region A in the (J-H/H-K) color-color diagram, Johnson et al. (2004) estimate a larger A_V in the range 2-4. Finally, the comparison of $Q_{Ly\alpha}$ from the radio emission to that deduced from the $B\gamma$ line gives a still larger value, $A_V = 8$ (Johnson et al. 2004). There thus appears to be a systematic increase of the derived extinction with increasing wavelengths. These differences may be due to a variety of causes such as: (1) mixing between the emission and absorption regions; (2) the coexistence of sources with different extinction within the Spitzer beam; or (3) the clumpy distribution of the absorbing material. For lack of a better spatial resolution in the infrared, it is impossible to distinguish among these possibilities, although we do know that region A comprises three components in the radio. That we can model the complete NIR-FIR SED with a characteristic opacity in the intermediate range of the observationally determined extinctions suggests that our model is representative of the *average* situation in region A.

From the dust properties and the physical size of the system, we can compute the total dust mass which we find to be $1.5 \times 10^6 M_\odot$. This is again a large dust mass for embedded clusters, which generally are one order of magnitude less massive. It is however a quite reasonable mass for a dust cloud in the general ISM of Haro 3. Indeed, based on the observations of Meier et al. (2001) and Gordon & Gottesman (1981), Johnson et al. (2004) have derived a total molecular and atomic gas mass of $\sim 6.7 \times 10^8 M_\odot$. Thus Haro 3 has a dust-to-gas ratio of 2.2×10^{-3} , consistent with the metallicity trends for BCDs illustrated by Hunt et al. (2005) and references therein.

To summarize, a model where the stellar clusters in region A heat an extended and diffuse region of the ISM of Haro 3 can account well for the NIR-FIR spectral energy distribution of the galaxy.

6. Star Formation in Haro 3

Star formation in Haro 3 occurs primarily in several knots distributed over the central region of the galaxy around the dust lane. The primary star-forming regions, knots A, B, and C (see Fig. 1) show different properties in the optical, the infrared, and the radio. Because of the compact radio emission found by Johnson et al. (2004), we would like to argue that knot A is a ensemble of star clusters with generally large extinction (the extinction is highly variable), while knot B is older and less obscured. Knot C, with its seemingly high PAH fraction, would be older still, with an $H\alpha$ flux ~ 6 times smaller than the other two knots, but with similar extinction (Steel et al. 1996). Because of its high density ($n_e \sim 200 \text{ cm}^{-3}$ Steel et al. 1996; Izotov & Thuan 2004) and compact size in the radio (Johnson et al. 2004), we would classify knot A as “active” (see the definition of this term in Hirashita & Hunt 2004). Such conditions are found also in mergers, with consequently a high pressure, and possible formation of super star clusters. That knot A is forming

stars in an “active” mode is corroborated by the good fit of the *DUSTY* model to the IR SED, the significant IR luminosity, and the relatively high SFR inferred by Johnson et al. (2004) from the radio emission. Knots B and C, on the other hand, are less dense ($n_e \sim 100 \text{ cm}^{-3}$ Steel et al. 1996), and can be considered as ”passive”.

The properties of the knots differ in terms of their IRAC and MIPS colors, but the IRS spectrum encompasses variable fractions of knots A and B, as well as the intervening ISM in the dust lane dividing the two regions. Were knot A to be an isolated dusty star cluster with a rising-spectrum radio source, we would expect it to have little or no PAH emission (Hunt et al. 2005) because we would expect the PAHs to be destroyed by the intense radiation field in the “active” compact region. However, we do see PAH emission. Therefore either our hypothesis is mistaken, namely PAHs can be found in compact dense star-forming regions, or our spectrum is “contaminated” by region B and the global ISM in Haro 3 (or both). To distinguish among the various possibilities, more extensive samples are needed, with a wide range of metallicities, luminosities, and PAH properties.

Haro 3 is relatively nearby BCD, only slightly metal deficient, with $12+\log(\text{O/H}) = 8.32$, and only slightly sub-luminous, with $M_B = -17.9$. Hence, it is an object which could serve as a transition case to link the properties of low-metallicity BCDs with those of more luminous metal-rich starbursts. Indeed, the EWs of its PAHs are generally higher than those of other BCDs (e.g. Wu et al. 2006), more consistent with more luminous and metal-rich starburst galaxies (Brandl et al. 2004). On the other hand, the PAHs in Haro 3 tend to be neutral according to the diagnostic diagram of Draine & Li (2001), more similar to “normal” galaxies than to starbursts. PAHs in BCDs may also be narrower than those of starbursts, and more similar to nearby HII regions although the differences may not be significant. The problem with many of these results is that their exact interpretation depends on the fraction of the global ISM in the IRS slits. These appear to cross the dust lane that separates the apparent positions of star-forming knots A and B, so we could be seeing a PAH contribution from the general ISM, not necessarily associated with the star formation. The PAH parameters also depend on how they were derived (e.g., continuum determination, profile templates, etc.). Consequently, on the basis of a single object, we cannot make definitive statements about low-metallicity PAHs, and must wait for larger BCD and starburst samples analyzed in a homogeneous way.

7. Summary

We present here the first results of our *Spitzer* Cycle 1 program which is aimed at the investigation of star formation in metal-poor BCD galaxies. We wish to study how star formation parameters and dust properties change as a function of metallicity and excitation. In this first paper of a series, we discuss the infrared properties of the most metal-rich object in our sample, Haro 3 = NGC 3353 = Mrk 35, with an oxygen abundance of $12+\log(\text{O/H}) = 8.32$. We have obtained IRS low and high-resolution spectra for the brightest star-forming region A in Haro 3, as well as IRAC images at 4.5 and $8 \mu\text{m}$ and MIPS images at 24, 70, and $160 \mu\text{m}$ of the galaxy. We

obtain the following results:

- (1) The IRS spectrum (Fig. 3) shows strong Polycyclic Aromatic Hydrocarbon (PAH) molecular emission, with features clearly detected at 5.7, 6.2, 7.7, 8.6, 11.2, 12.7, and $16.4\mu\text{m}$. The PAHs in Haro 3 are predominantly neutral and small, similar to those found in normal spiral galaxies, suggesting that they reside in the general ISM and not in the star-forming region A. The PAH emission features are relatively narrow and their equivalent widths are generally high for the metallicity of Haro 3.
- (2) Gaseous nebular line emission is also seen. The IRS spectrum shows several fine-structure lines, including $[\text{S IV}]\lambda 10.51$, $[\text{Ne II}]\lambda 12.81$, $[\text{Ne III}]\lambda 15.55$, 36.01 , $[\text{S III}]\lambda 18.71$, 33.58 , $[\text{O IV}]\lambda 25.89$, and $[\text{Si II}]\lambda 34.82\mu\text{m}$.
- (3) Several fairly high-excitation lines are detected in Haro 3. The faint $[\text{O IV}]$ line at $25.89\mu\text{m}$ indicates the presence of radiation as hard as 54.9 eV in Haro 3. This hard radiation is perhaps due to the Wolf-Rayet stars present in the galaxy. Such a detection is intriguing because the high-ionization $[\text{Fe V}]\lambda 4227$ and $\text{HeII }\lambda 4686$ emission lines which both have an ionization potential of 54.4 eV , are not seen in the optical spectrum of Haro 3, presumably because of extinction effects. The electron density derived from the MIR lines is about half that derived from the optical lines. Moreover HII photoionization CLOUDY models that reproduce the optical line intensities predict MIR lines that are systematically too small compared to those observed. This discrepancy may be understood if the beam dilution in the IR is taken into account, and if the bulk of the MIR radiation comes from a region more obscured than the optical one.
- (4) Like most galaxies, Haro 3 is a composite entity in the IR. We see *extended* stellar photospheric emission and *compact* hot dust continuum at $4.5\mu\text{m}$ coming mainly from the star-forming regions, *extended* PAH emission coming mainly from the general ISM at $8\mu\text{m}$, with a small contribution from hot dust continuum and stars, *compact* small grain warm dust emission associated with active star-forming regions at 24 and $70\mu\text{m}$, and cooler *extended* dust emission associated with older stellar populations at $160\mu\text{m}$.
- (5) We have modeled the IR spectral energy distribution (SED) of star-forming region A with *DUSTY*, a code which solves the radiative transfer problem in a dust envelope. The best-fit model gives a total luminosity of $2.8\times 10^9\text{ L}_\odot$ and a total stellar mass of $2.8\times 10^6\text{ M}_\odot$ for the ionizing star clusters. These numbers are not unreasonably high because region A contains at least three star clusters. The best-fit age of the star formation burst in A is 5 Myr , in agreement with the age derived from the optical SED. The number of ionizing photons is $4.4\times 10^{52}\text{ photons s}^{-1}$, greater than the one derived from the $\text{Br}\gamma$ line but smaller than that derived from the thermal radio flux, indicating more extinction in the $\text{Br}\gamma$ flux than in the MIR.
- (6) As for the nature of the dust, the best-fit *DUSTY* model implies that silicates are absent from region A. The maximum grain size can reach the very large value of $40\mu\text{m}$ if we attempt to fit the $160\mu\text{m}$ MIPS flux. However, we obtain more reasonable results ($\sim 1\mu\text{m}$) if we consider the $160\mu\text{m}$ flux to be an upper limit and do not attempt to fit it. The Av of the dust given by *DUSTY* is $\lesssim 3$,

higher than the value of 0.5 derived from the optical lines, and lower than the value of ~ 8 derived from radio observations, consistent with the picture that observations at longer wavelengths probe more deeply into the star-forming region. The dust density does not vary with distance from the central clusters, and the dust extent is 430 pc in radius, considerably larger than region A. This suggests that the geometry deduced from the *DUSTY* modeling is that of a large cloud of dust in the general ISM of Haro 3, surrounding region A and heated by the clusters in it, rather than that of a giant dust shell around region A.

This work is based on observations made with the Spitzer Space Telescope, which is operated by the Jet Propulsion Laboratory, California Institute of Technology, under NASA contract 1407. We would like to thank Yanling Wu and Jim Houck for astute comments, and an anonymous referee for a careful reading and insightful suggestions which improved the paper. Support for this work was provided by NASA through contract GG10638 issued by JPL/Caltech. T.X.T. and Y.I.I. acknowledge partial financial support from NSF grant AST 02-05785. T.X.T. is grateful for the hospitality of the Service d’Astrophysique at Saclay and of the Institut d’Astrophysique in Paris during his sabbatical leave. He thanks the University of Virginia for the award of a Sesquicentennial Fellowship. This research has made extensive use of the NASA/IPAC Extragalactic Database (NED), operated by the Jet Propulsion Laboratory, California Institute of Technology, under contract with the National Aeronautics and Space Administration.

REFERENCES

Anders, E., & Grevesse, N. 1989, *Geochim. Cosmochim. Acta*, 53, 197

Armus, L., et al. 2004, *ApJS*, 154, 178

Asplund, M., Grevesse, N., & Sauval, A. J. 2005, *ASP Conf. Ser.* 336: Cosmic Abundances as Records of Stellar Evolution and Nucleosynthesis, 336, 25

Brandl, B. R., et al. 2004, *ApJS*, 154, 188

Calzetti, D., Meurer, G. R., Bohlin, R. C., Garnett, D. R., Kinney, A. L., Leitherer, C., & Storchi-Bergmann, T. 1997, *AJ*, 114, 1834

Draine, B. T. 2006, private communication

Draine, B. T., & Li, A. 2001, *ApJ*, 551, 807 1

Engelbracht, C. W., Gordon, K. D., Rieke, G. H., Werner, M. W., Dale, D. A., Latter, W. B. 2005, *ApJ*, 628, 29

Fazio, G. G., et al. 2004, *ApJS*, 154, 10

Ferland, G.J. 1996, Hazy: A brief Introduction to CLOUDY (Univ. Kentucky Dept. Phys. Astron. Internal Rep.)

Ferland, G.J., Korista, K.T., Verner, D.A., Ferguson, J.W., Kingdon, J.B., & Verner, E.M. 1998, *PASP*, 110, 761

Genzel, R., & Cesarsky, C. 2000, *ARA&A*, 38, 761

Gil de Paz, A., Madore, B. F., & Pevunova, O. 2003, *ApJS*, 147, 29

Gordon, D., Gottesman, S. 1981, *AJ*, 86, 161

Gordon, K. D., et al. 2005, *PASP*, 117, 503

Guseva, N. G., Izotov, Y. I., & Thuan, T. X. 2006, *ApJ*, 644, 890

Helou, G., Lu, N. Y., Werner, M. W., Malhotra, S., & Silbermann, N. 2000, *ApJ*, 532, L21

Hirashita, H., & Hunt, L. K. 2004, *A&A*, 421, 555

Hogg, D. W., Tremonti, C. A., Blanton, M. R., Finkbeiner, D. P., Padmanabhan, N., Quintero, A. D., Schlegel, D. J., & Wherry, N. 2005, *ApJ*, 624, 162

Houck, J. R., et al. 2004a, *ApJS*, 154, 18

Houck, J. R., et al. 2004b, *ApJS*, 154, 211

Hughes, D.H., et al. 1998, *Nature*, 394, 241

Hunt, L., Bianchi, S., & Maiolino, R. 2005, *A&A*, 434, 849

Hunt, L. K., & Maiolino, R. 2005, *ApJ*, 626, L15

Hunt, L.K., Vanzi, L., & Thuan, T.X. 2001, *A&A*, 377, 66

Ivezić, Z., Nenkova, M., & Elitzur, M. 1999, User Manual for DUSTY, University of Kentucky Internal Report, accessible at <http://www.pa.uky.edu/~moshe/dusty>

Ivezić, Z. & Elitzur, M. 1997, *MNRAS*, 287, 799

Izotov, Y.I., & Thuan, T. X. 2004, *ApJ*, 602, 200

Johnson, K. E., Indebetouw, R., Watson, C., & Kobulnicky, H. A. 2004, *AJ*, 128, 610

Leitherer, C., et al. 1999, *ApJS*, 123, 3

Li, A., & Draine, B. T. 2001, *ApJ*, 554, 778

Loose, H.-H. & Thuan, T.X. in Star-Forming Dwarf Galaxies and related objects, eds. D. Kunth, T.X. Thuan & J.T.T. Van (Gif-sur-Yvette: Editions Frontieres), p. 73

Makovoz, D., & Marleau, F. R. 2005, PASP, 117, 1113

Malkan, M. A., Gorjian, V., & Tam, R. 1998, ApJS, 117, 25

Mathis, J. S., Rumpl, W., & Nordsieck, K. H. 1977, ApJ, 217, 425

Meier, D. S., Turner, J. L., Crosthwaite, L. P., Beck, S. C. 2001, AJ, 121, 740

Men'shchikov, A. B., Schertl, D., Tuthill, P. G., Weigelt, G., Yungelson, L. R. 2002, A&A, 393, 867

Metcalfe, L., et al. 1996, A&A, 315, L105

Plante, S., & Sauvage, M. 2002, AJ, 124, 1995

Rieke, G. H., et al. 2004, ApJS, 154, 25

Sanders, D. B., Mirabel, I. F. 1996, ARA&A 34, 749

Schaerer, D., & de Koter, A. 1997, A&A, 322, 598

Smith, J.D., Draine, B. T., et al. 2006, ApJ, submitted

Steel, S. J., Smith, N., Metcalfe, L., Rabbette, M., & McBreen, B. 1996, A&A, 311, 721

Steidel, C.C., Adelberger, K.L., Shapley, A.E., et al. 2003, ApJ, 592, 728

Thuan, T.X., & Izotov, Y.I. 2005, ApJS, 161, 240

Thuan, T.X., Sauvage, M., & Madden, S. 1999, ApJ, 516, 783

Vanzi, L., Sauvage, M. 2004, A&A, 509

Verma, A., Lutz, D., Sturm, E., Sternberg, A., Genzel, R., & Vacca, W. 2003, A&A, 403, 829

Weedman, D. W., Le Floc'h, E., Higdon, S. J. U., Higdon, J. L., & Houck, J. R. 2006, ApJ, 638, 613

Werner, M. W., et al. 2004, ApJS, 154, 1

Whitmore, B. C., Zhang, Q. 2002, AJ, 124, 1418

Wu, Y., Charmandaris, V., Hao, L., Brandl, B. R., Bernard-Salas, J., Spoon, H. W. W., & Houck, J. R. 2006, ApJ, 639, 157

Table 1. IRAC and MIPS total fluxes of Haro 3 with Other Published Photometry

Telescope/Instrument	Wavelength (μm)	Total flux (mJy)
Spitzer/IRAC	4.509	20.7 ± 2.1
”	7.982	148.0 ± 14.8
Spitzer/MIPS	23.7	810 ± 81
”	71.0	3870 ± 387
”	156.0	3900 ± 390
IRAS ^a	12	211.1 ± 29.6
”	25	941.8 ± 56.5
”	60	4949.0 ± 395.9
”	100	6746.0 ± 404.8
ISO/ISOCAM ^b	7.75	149 ± 30
”	15.0	300 ± 70
WIYN/NIRIM ^c	1.26	1.19 ± 0.12
”	1.65	1.12 ± 0.11
”	2.12	1.06 ± 0.11
VLA ^c	13000	2.96 ± 0.22
”	36000	2.60 ± 0.22

^aFrom NED.^bFrom Metcalfe et al. (1996).^cFrom Johnson et al. (2004) for A1+A2.

Table 2. PAH Parameters Obtained by Fitting Lorentzian Profiles

Wavelength ^a (μm)	Integrated ^b Flux ($10^{-16} \text{ W m}^{-2}$)	Equivalent ^b Width (μm)	FWHM ^b (μm)
6.202	8.3 (0.3)	1.31 (0.22)	0.17 (0.004)
7.693	26.0 (9.2)	2.85 (1.47)	0.66 (0.11)
8.631	6.4 (0.9)	0.64 (0.12)	0.38 (0.08)
11.269	8.3 (0.2)	0.60 (0.05)	0.25 (0.006)
12.814	6.3 (1.3)	0.32 (0.07)	0.13 (0.015)
16.424	1.2 (0.1)	0.06 (0.01)	0.18 (0.007)

^aFitted restframe wavelength, corrected for $z = 0.00323$.

^bStandard deviations of the repeated measurements are given in parentheses. The true uncertainty including calibration is probably $\sim 20\%$.

Table 3. Fine Structure Line Parameters Obtained by Fitting Gaussian Profiles

Line ^a	E_{ion} ^b (eV)	Nominal Wavelength (μm)	Fitted ^c Wavelength (μm)	Integrated ^d Flux ($10^{-16} \text{ W m}^{-2}$)	Equivalent ^d Width (μm)	FWHM ^d (μm)
[S IV]	34.8	10.511	10.510	3.01 (0.20)	0.21 (0.01)	0.022 (0.005)
[Ne II]	21.6	12.814	12.813	2.71 (0.05)	0.12 (0.01)	0.020 (0.001)
[Ne III]	41.0	15.555	15.556	7.51 (0.07)	0.31 (0.02)	0.022 (0.001)
[S III]	23.3	18.713	18.713	4.03 (0.01)	0.13 (0.01)	0.030 (0.001)
[O IV]	54.9	25.890	25.961	0.60 (0.02)	0.02 (0.01)	0.065 (0.002)
[S III]	23.3	33.481	33.439	10.6 (0.01)	0.22 (0.01)	0.055 (0.001)
[Si II]	8.2	34.815	34.800	4.80 (0.01)	0.10 (0.01)	0.056 (0.001)
[Ne III]	41.0	36.014	36.000	1.27 (0.07)	0.31 (0.02)	0.66 (0.11)

^aBecause of the presence of [Ar III] and [Ar II] only in the low-resolution spectra, we do not give their parameters here.

^bIonization potential (lower) of the stage leading to the transition.

^cRestframe, corrected for the $z = 0.00323$ (Thuan & Izotov 2005).

^dStandard deviations of the repeated measurements are given in parentheses. The true uncertainty including calibration is probably $\sim 20\%$.

Table 4. Chemical Composition of Regions A1 and A2 used in CLOUDY Calculations

Element	$\log \text{X/H}$
He	−1.07
C	−4.03
N	−4.93
O	−3.68
Ne	−4.53
Si	−5.13
S	−5.48
Cl	−7.03
Ar	−6.08
Fe	−5.78

Table 5. Comparison of Observed and Modeled Optical Relative Line Intensities in Region A1

Line	Observations ^a	CLOUDY ^a
3727 [O II]	2.4978	2.3101
3750 H12	0.0374	0.0314
3771 H11	0.0433	0.0407
3798 H10	0.0553	0.0542
3835 H9	0.0761	0.0746
3869 [Ne III]	0.3141	0.3191
4068 [S II]	0.0215	0.0225
4101 H δ	0.2817	0.2612
4340 H γ	0.4966	0.4705
4363 [O III]	0.0274	0.0272
4658 [Fe III]	0.0091	0.0094
4861 H β	1.0000	1.0000
4959 [O III]	1.3176	1.3660
5007 [O III]	4.0352	4.1118
5200 [N I]	0.0072	0.0052
5270 [Fe III]	0.0047	0.0054
5518 [Cl III]	0.0059	0.0061
5538 [Cl III]	0.0042	0.0044
5755 [N II]	0.0037	0.0039
6300 [O I]	0.0094	0.0504
6312 [S III]	0.0123	0.0120
6563 H α	2.9491	2.8930
6583 [N II]	0.2007	0.2025
6717 [S II]	0.1571	0.1991
6731 [S II]	0.1267	0.1506
7135 [Ar III]	0.0929	0.0888
7320 [O II]	0.0259	0.0288
7330 [O II]	0.0223	0.0234

^aRelative to H β .

Table 6. Comparison of the Observed and Predicted Relative Intensities of the MIR lines

Line	Observations A1+A2 ^a	Model			Obs./Model
		A1 ^b	A2 ^c	A1+A2 ^a	
10.51 [S IV]	0.26	0.15	0.08	0.11	2.4
12.81 [Ne II]	0.24	0.03	0.05	0.04	6.0
15.55 [Ne III]	0.66	0.40	0.37	0.38	1.7
18.71 [S III]	0.35	0.22	0.21	0.21	1.7
33.48 [S III]	0.92	0.43	0.41	0.42	2.2
34.82 [Si II]	0.42	0.20	0.28	0.25	1.6
36.01 [Ne III]	0.11	0.04	0.03	0.03	3.7

^aRelative to the total intensity of the H β emission line in regions A1+A2.

^bRelative to the intensity of the H β emission line in region A1.

^cRelative to the intensity of the H β emission line in region A2.

Table 7. Results from the *DUSTY* Fit

Parameter Name (1) ^a	Unit (2) ^b	Best fit value (3) ^c	Confidence range (4) ^d
Starburst age	Myr	5	—
Silicates abundance	%	0	0–5
Graphite abundance	%	67	55–77
Amorphous Carbon abundance	%	33	23–45
a(min)	μ m	0.008	0.006–0.010
a(max)	μ m	40.0	>10.8
Size distribution exponent	n.a.	4	—
R^{out}	pc	435	380–490
Density exponent in shell	n.a.	0	—
T_{int}	K	500	479–523
τ_V		3	2.8–3.3

^aParameter name.^bPhysical units of this parameter.^cBest-fit value (mean error per pseudo-filter band is 7%).^dRange within which the change of this parameter only will result in a mean error per pseudo-filter band of 10%. A — corresponds to values which are so tightly constrained by our fit that any change in them results in a mean error of >10%.

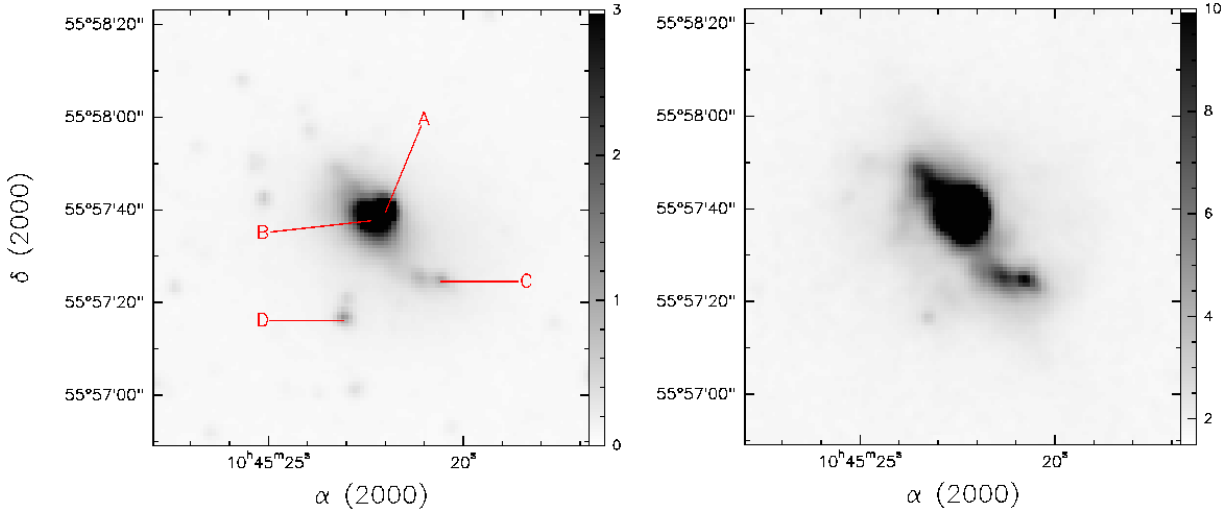


Fig. 1.— The $4.5\mu\text{m}$ (IRAC2) image (left panel) and the $8.0\mu\text{m}$ (IRAC4) image (right panel) of Haro 3. The units given in the colorbar are MJy/sr. The star-forming knots identified by Steel et al. (1996) are labeled.

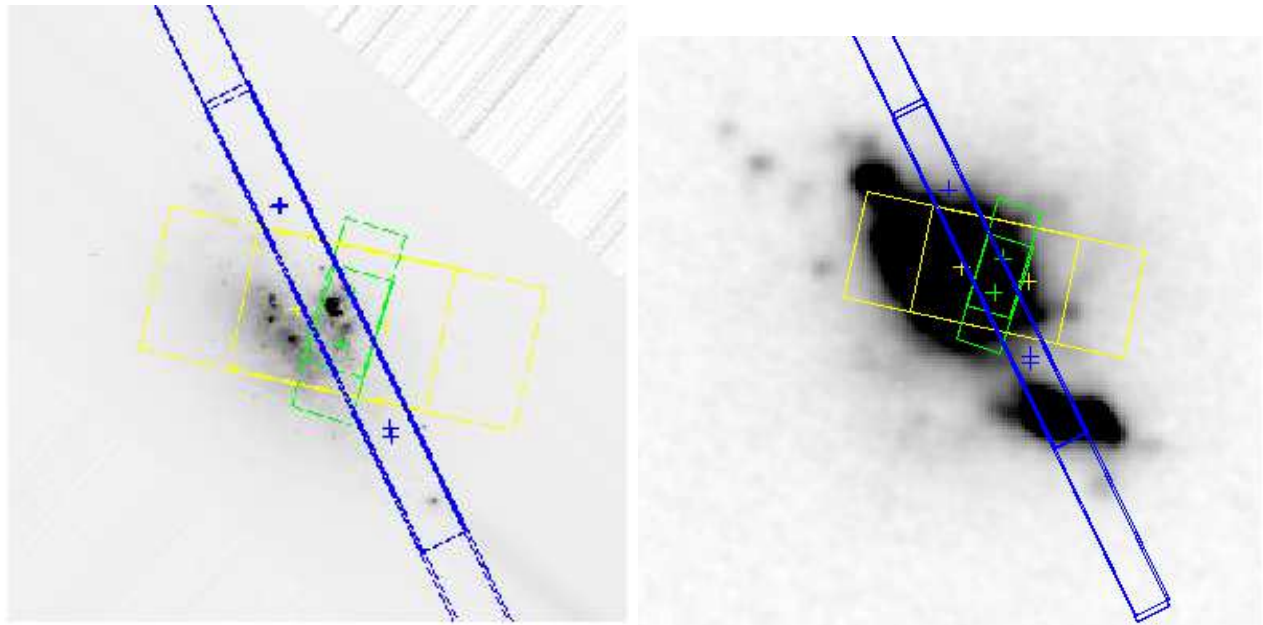


Fig. 2.— The IRS slit positions overlaid on the *HST*/WFPC2 image (left panel, Malkan et al. (1998)) and the $H\alpha$ image (right panel, Gil de Paz et al. 2003) of Haro 3. Images are oriented North up, East left; the long (SL) IRS slit is $57'' \times 3''.6$ (blue), the SH slit $4''.7 \times 11''.3$ (green), and the LH slit $11''.1 \times 22''.3$ (yellow).

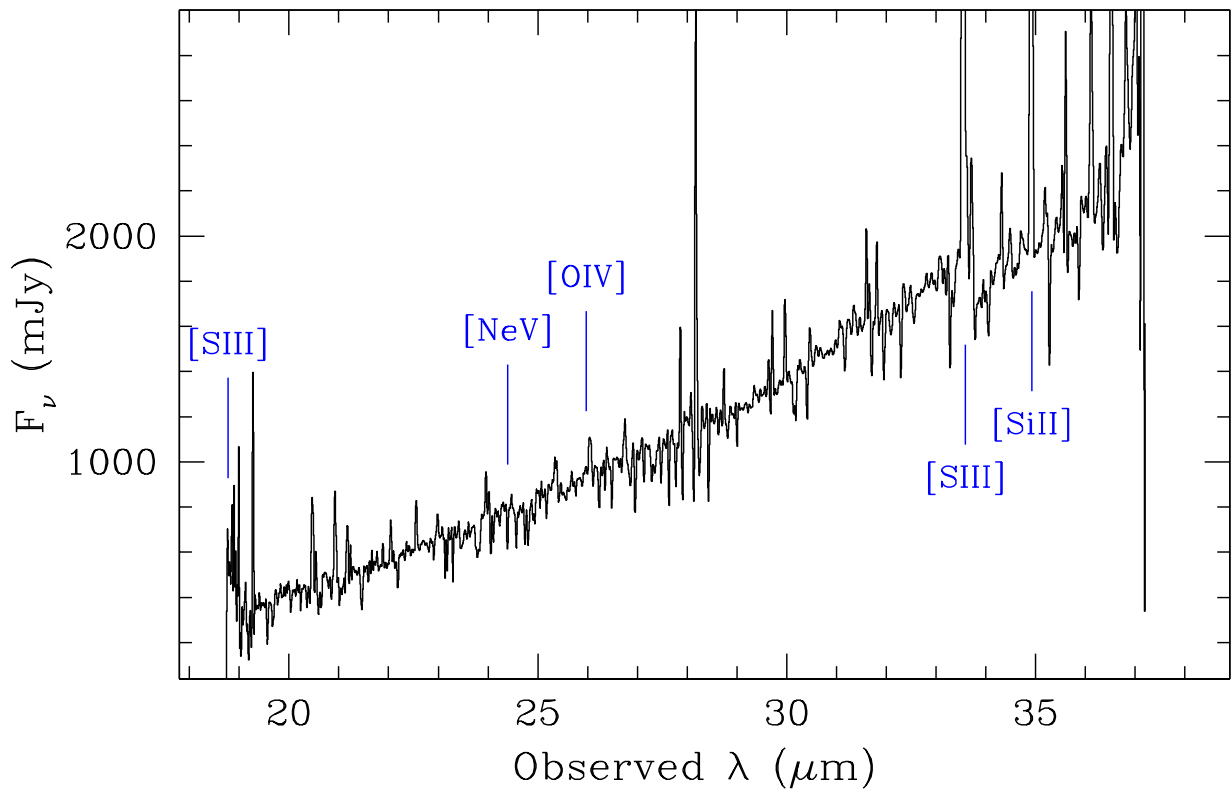
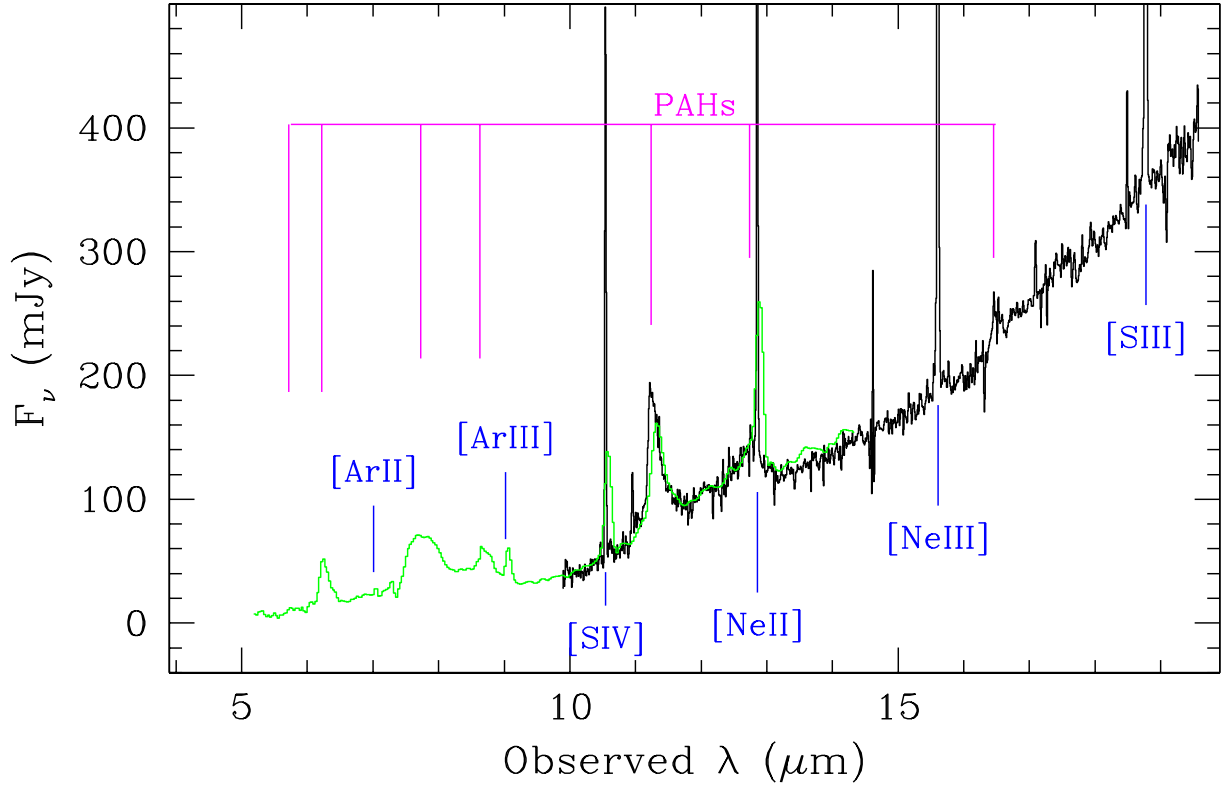


Fig. 3.— The IRS spectrum of Haro 3 consisting of the short-wavelength low-resolution mode and both high-resolution modes: SL+SH are shown in the upper panel, and LH in the lower one. The PAH features at 5.7, 6.2, 7.7, 8.6, 11.2, 12.7, and 16.4 μm are clearly detected, as are several emission lines: [S IV], [Ne II], [Ne III], [S III], [O IV].

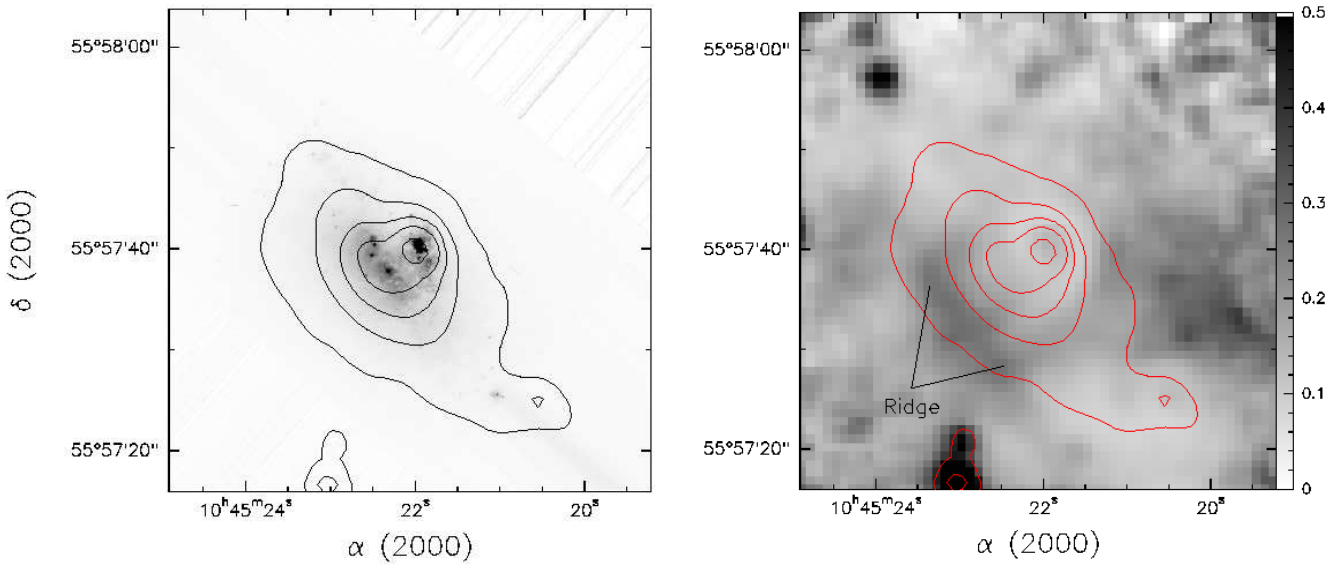


Fig. 4.— The 4.5 μ m IRAC image of Haro 3 (see Fig. 1) contoured on the (left panel) *HST*/WFPC2 F606W image (Malkan et al. 1998) and on the 4.5/8.0 μ m flux ratio (right panel). Contours range from 2, 5, 10, 20, 45, 70, 95% of the 4.5 μ m peak; the “ridge” feature referred to in the text is marked. The bright optical point source is clearly coincident with the 4.5 μ m brightness peak. The 4.5/8.0 μ m ratio changes by a factor of 10 over the image.

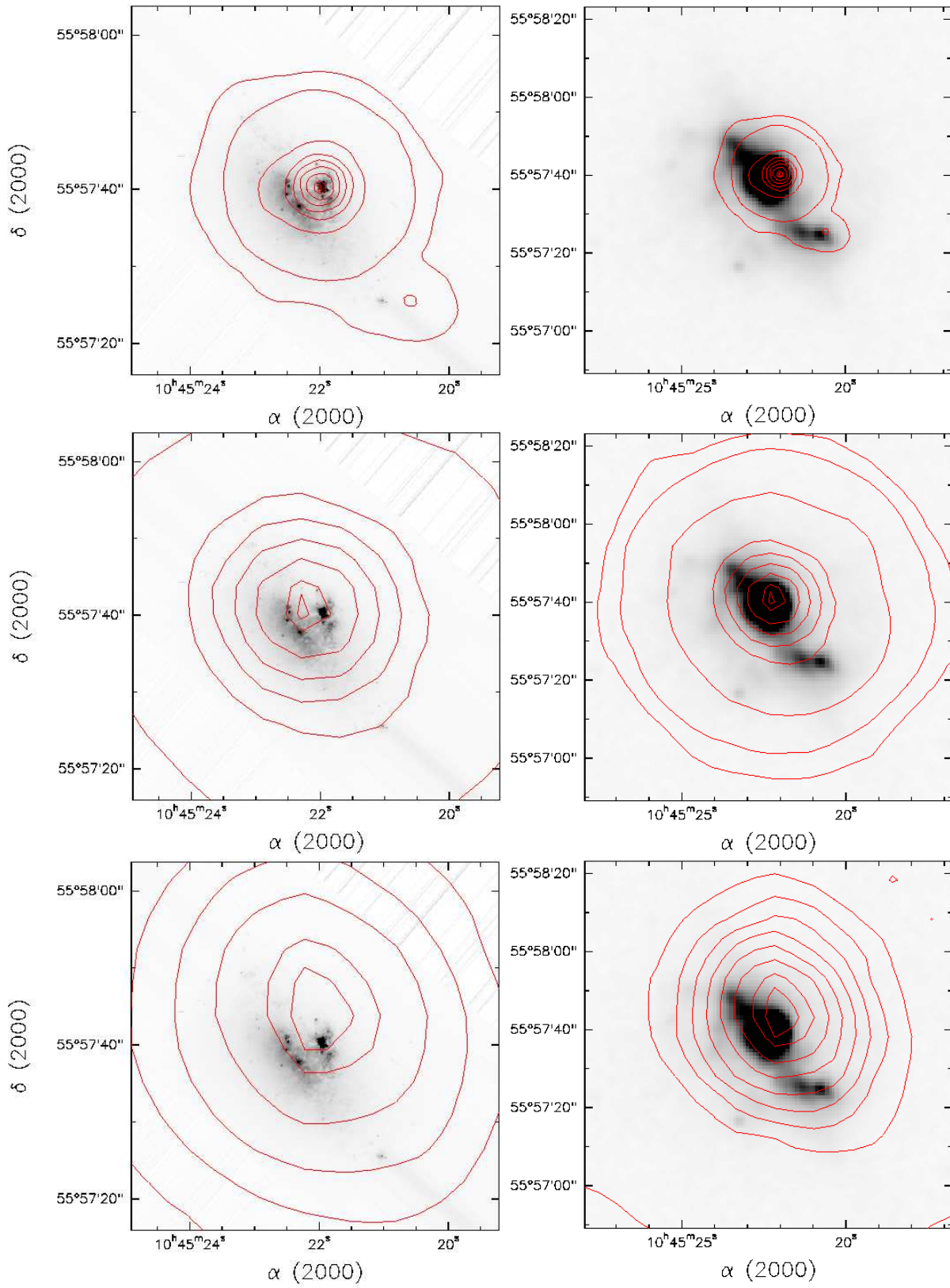


Fig. 5.— The 24 μm (top panel), 70 μm (middle), and 160 μm (bottom) MIPS images of Haro 3 contoured on the (left panels) HST/WFPC2 F606W image (Malkan et al. 1998), and on the 8.0 μm IRAC image (right). Contours run 1% above the sky, then 8%, 15, 30, 45, 60, 75, 90, and 95% of peak value, except for MIPS 160, where they run from 10% above the sky, then 30 to 90% (in increments of 10%), and 95% of peak value.

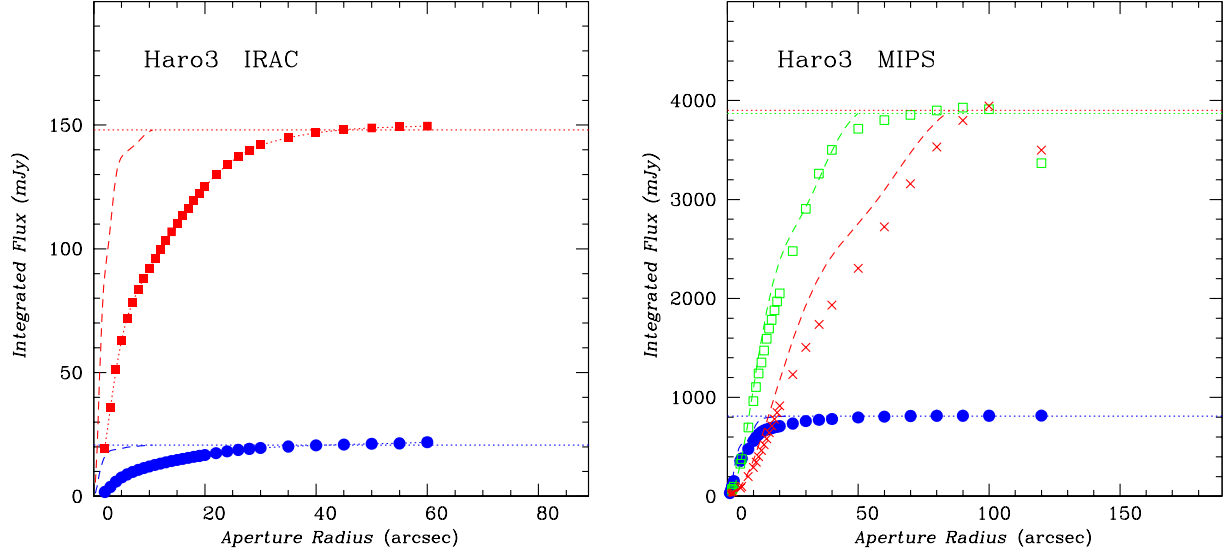


Fig. 6.— Growth curves for IRAC (left panel) and MIPS (right) photometry. In both panels, the horizontal dotted line traces the adopted total flux from Haro 3, and the dashed line represents the point-response function. In the left panel, IRAC channel 2 is indicated by filled circles, channel 4 by filled squares. In the right panel, MIPS-24 is shown by filled circles, MIPS-70 by open squares, and MIPS-160 by \times . Haro 3 is extended at shorter wavelengths and possibly at $160\mu\text{m}$, but appears virtually point-like at 24 and $70\mu\text{m}$.

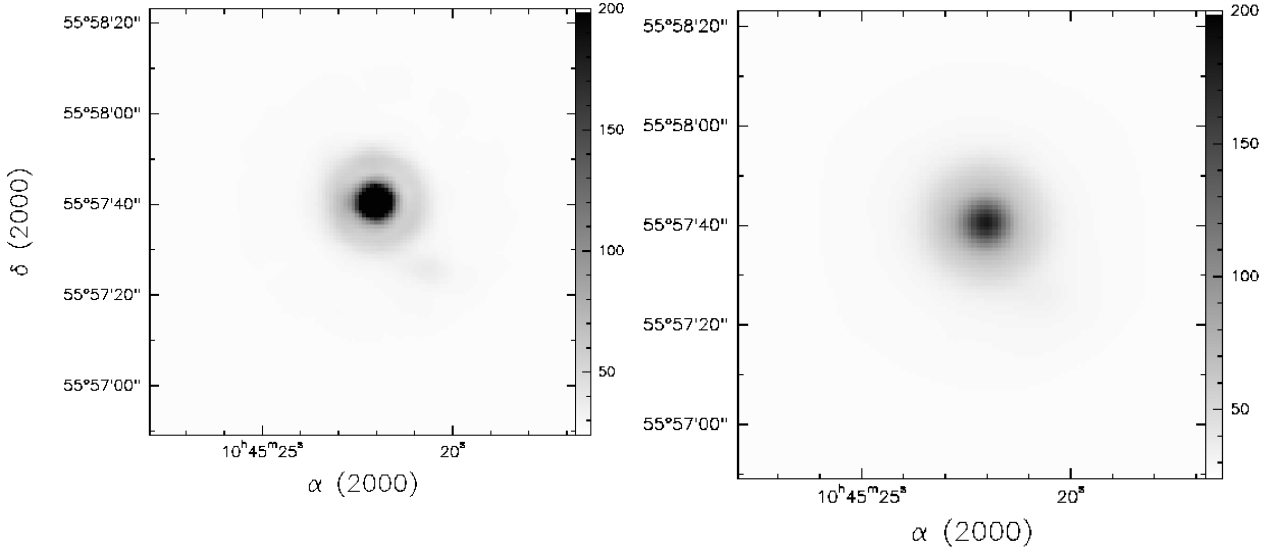


Fig. 7.— The $24\mu\text{m}$ mosaic of Haro 3 before (left panel) and after (right panel) deconvolution. Units of the colorbar are MJy/sr .

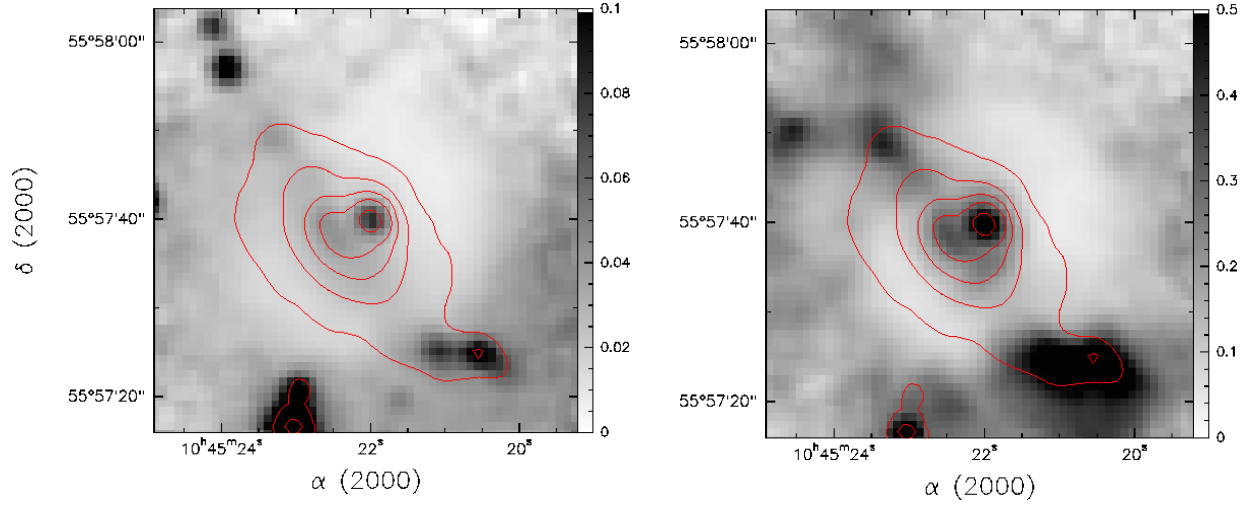


Fig. 8.— Contours of the $4.5 \mu\text{m}$ image superimposed on the $4/24 \mu\text{m}$ flux ratio (left panel), and on the $8/24 \mu\text{m}$ flux ratio (right panel). The $24 \mu\text{m}$ image has been deconvolved.

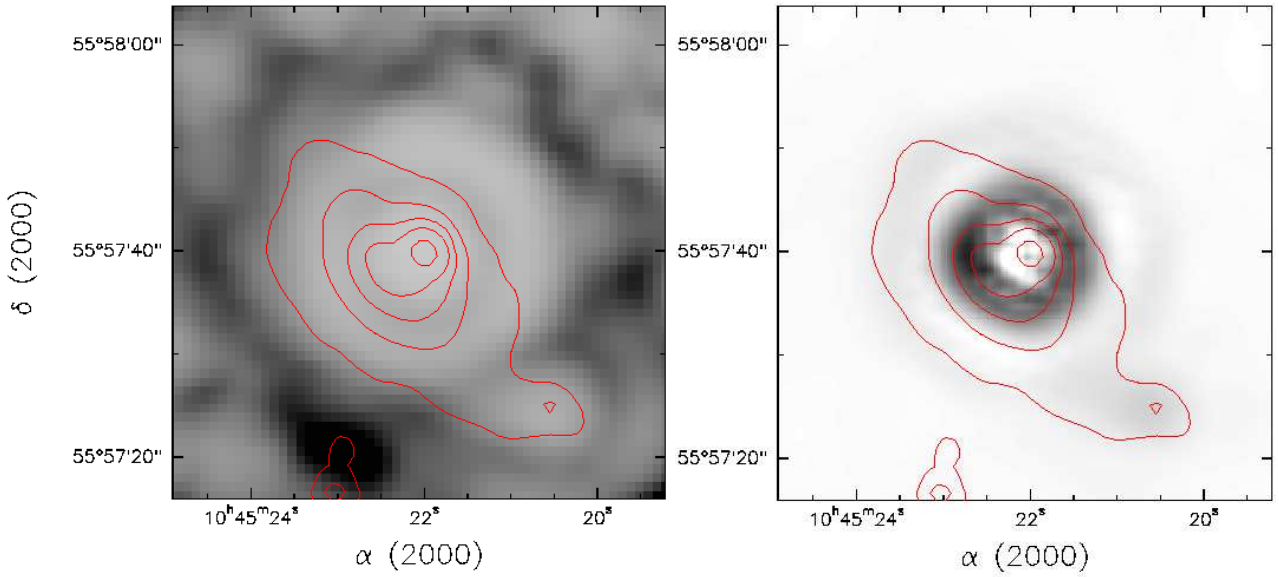


Fig. 9.— Results of two manipulations of the MIPS-24 image. The left panel shows the $8 \mu\text{m}$ image convolved with the MIPS-24 PRF, then divided by the original $24 \mu\text{m}$ image; the right panel gives the $24 \mu\text{m}$ image obtained by subtracting the MIPS-24 PRF from the original $24 \mu\text{m}$ image. In both panels, the IRAC $4.5 \mu\text{m}$ is overlaid in contours as in Fig. 4; intensity grows from white to black.

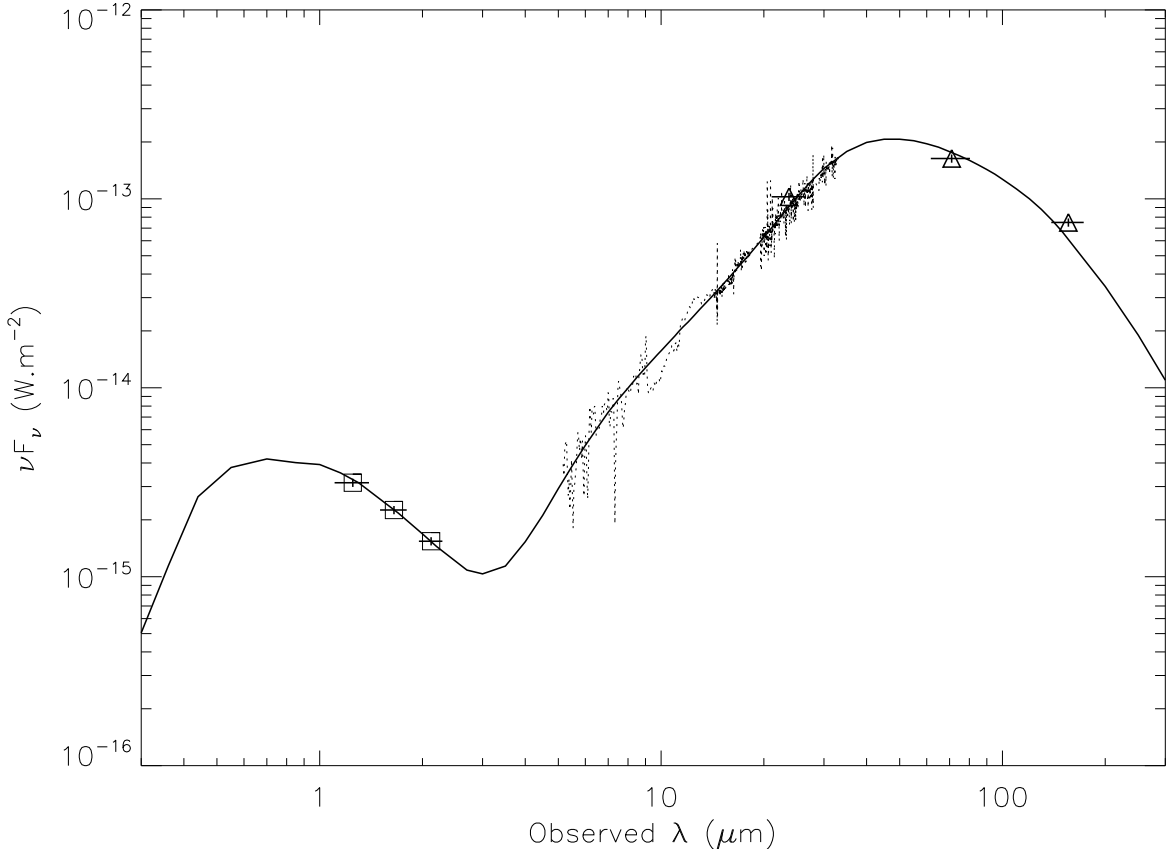


Fig. 10.— The *DUSTY* fit to the spectral energy distribution of region A in νF_ν vs. λ . The thick continuous line in the model spectrum has been normalized by the median ratio between the observed and model fluxes. The open squares represent the NIR photometry while the open triangles represent MIPS. For both datasets, the horizontal bar shows the width of the filter while the vertical bar, generally smaller than the symbol, is the error bar. The dotted line is the IRS spectrum from which the PAH features and main ionic lines have been subtracted.